water

MDPI

Article

Conceptual Evaluation of Factors Controlling Groundwater Chemistry in Ad-Dawadmi, Saudi Arabia, Using Visualization and Multiple Lines of Evidence

Hassan E. Gomaa [1,2,*], AbdAllah A. Alotibi [1], Mohamed Charni [3,4], Abdulhadi H. AlMarri [5] and Fatma A. Gomaa [1,6,*]

1 Department of Chemistry, College of Science and Humanities, Shaqra University, Ad-Dawadmi 11911, Saudi Arabia; aalotaibi@su.edu.sa
2 Department of Nuclear Safety Engineering, Nuclear Installations Safety Division, Atomic Energy Authority, Cairo 11765, Egypt
3 Department of Biology, College of Science and Humanities, Shaqra University, Ad-Dawadimi 11911, Saudi Arabia; mcharni@su.edu.sa
4 Laboratory of Biodiversity, Parasitology, and Ecology of Aquatic Ecosystems LR18ES05, Faculty of Sciences of Tunis, University of Tunis El Manar, Tunis 2092, Tunisia
5 Department of Chemistry, College of Alwajh, Tabuk University, Tabuk 71421, Saudi Arabia; aalmarri@ut.edu.sa
6 Departement of Chemistry, College of Women for Science, Arts, and Education, Ain Shams University, Cairo 11757, Egypt
* Correspondence: hjomaah@su.edu.sa or hassan_emgh@yahoo.com (H.E.G.); fjomaah@su.edu.sa or fatma_emgh@yahoo.com (F.A.G.)

Abstract: Understanding the hydrogeochemical and physicochemical processes and factors controlling the chemical characteristics of groundwater (GW) is essential in water resources studies. In this work, the authors explored, applied, and evaluated the practicality of a series of analysis methods, exploring their ability to improve the representation of the generic GW chemical datasets. The demonstration resulted in a detailed explanation of findings and interpretations, which benefits newcomers who may not be experts in managing such data. Visualization-based, facile, readily readable, and interpretable graphs were tuned and applied to identify the interconnected controlling factors. The examined varieties were bubble diagrams, 3D surface plots, and scatter box plot matrices. Box plot matrices yielded intensive information about the significant interacting parameters in one graph. Employing bubble diagrams produced vast detail, allowing the identification of the significant processes and enabling the recognition of internally acting mechanisms that were otherwise hidden. The identified GW evolution processes include aerosol dissolution, evaporation, direct and reverse ion exchange, precipitation of calcium salts, flushing out of soil-bounded salts, and rock weathering. pH and HCO_3^- fluctuations coupled with evaporation were recognized as prominent factors giving rise to the vicious salinization cycle, which is thought to be the process causing the worst deterioration in the GW quality and the salinity within the study area.

Keywords: GW; salinization; box plot matrix; bubble diagram; Saudi Arabia

Citation: Gomaa, H.E.; Alotibi, A.A.; Charni, M.; AlMarri, A.H.; Gomaa, F.A. Conceptual Evaluation of Factors Controlling Groundwater Chemistry in Ad-Dawadmi, Saudi Arabia, Using Visualization and Multiple Lines of Evidence. *Water* **2022**, *14*, 1857. https://doi.org/10.3390/w14121857

Academic Editor: Dimitrios E. Alexakis

Received: 10 May 2022
Accepted: 7 June 2022
Published: 9 June 2022

1. Introduction

Groundwater (GW) represents water resources for different daily life activities and plays an essential ecological function in public health and economic value. The survival of natural habitats, such as forests, grasslands, vegetation in general, and animal species, depends on the availability of an adequate quantity of suitable quality water. The water content of the soil is also a significant factor in preventing soil erosion and adverse changes in its chemical composition. Therefore, it is clear that the ecosystem on the land's surface depends on GW for survival. GW can be considered to be a natural water bank due to its

capacity to act as a buffer, which is available when rainfall is low or absent, and is later recharged by rainfall. Globally speaking, GW is a crucial natural resource for present and future generations, and is predominant.

In some cases, including in the considered study area, GW is the sole source of water in hyper-arid, arid, and even semi-arid regions [1]. Moreover, according to the World Health Organization (WHO), about 80% of all diseases in human beings are caused by water. The lack of hydrogeochemical studies in such areas contributes to limiting the knowledge and evaluation of the chemistry state of GW. This limitation is significant when extra factors, such as minimal precipitation (prolonged drought periods), urbanization, irrigation and landscaping, and overexploitation of GW resources, may adversely impact the aquifer quality [2–6].

Assessing the chemistry of GW helps understand the GW evolution, characterize the dominant geochemical interactions, and recognize the anthropogenic effects [7]. In addition, the climate, the rocks' weathering, and the percolation through and contact with the lithologic soils enhance the dissolution and accumulation of ions into the aqueous environment, which is exacerbated during the long dry seasons that have become more frequent in hyper-arid regions as a result of climatic change [8–10]. The chemical species are not randomly allocated throughout the GW system, but are instead governed by the diagenesis reactions, chemical exchange, and mass transfer processes. Diagenesis reactions include dolomitization/dedolomitization, recrystallization, cementation, GW movement-driven solubilization, and re-precipitation of minerals. The interactions of water chemistry, hydrology, sedimentology, and mineralogy manifest physically in modifying the landscape, karst lineaments, permeability and porosity distribution, and the establishment and operation of local and regional flow systems. The processes controlling the resultant GW chemical character have only been highlighted [11]. Therefore, characterizing and understanding the GW system chemistry factors is vital in integrated water management plans and strategies [12–14].

All these data need to be analyzed to understand the functioning of the water bodies to determine evolution trends and, eventually, define management actions. The tools used to assess the effects of such interconnected factors on the quality of resources aid in securing fit-for-purpose water for the activities and populations that depend on it. Hence, there are many different ways to focus on GW interpretation, and a large number of techniques, tools, and applications that can be used to achieve these objectives [15]. Each study has its design objectives and questions to be answered that determine the tools' usage. Other equally important determinants for selecting the tools are the availability and proof of their usefulness, ease of application, readability, direct interpretability, level of expertise (available and needed), time and cost frames, completeness of site-relevant data, etc.

Demarcating the mechanisms controlling the evolution of a GW system and estimating the relative contributions of such processes (e.g., weathering, dissolution, evaporation, and irrigation water return flow) is a multidisciplinary and complicated task. Nevertheless, some wet chemistry-based interpretations may aid significantly in forecasting and determining the prominent processes. For example, concentrations of Cl^- Na^+, SO_4^{2-}, Mg^{2+}, Ca^{2+}, and HCO_3^- (conservative, quasi-conservative, and nonconservative ions, respectively) are nevertheless significant in determining the hydrogeochemical evolution of the GW system, such as solubilization/precipitation, forward and reverse cation exchange, and incongruent silicate mineral reactions. Rainfall levels, coupled with the other controlling lithological factors, affect the recharging of aquifers and, hence, the respondent hydrogeochemical quality conditions [1,16].

The main aim of hydrogeochemical studies is to describe the geochemical characteristics, properties, and principles that control the behavior of dissolved constituents in the system under consideration. The spatial and temporal distribution of the concentrations of the reactive constituents may vary within the recharge area, evolve in the flow direction, and be governed by the history of solute concentrations delivered via recharge and subsequent inter-aquifer mixing, along with flow systems [1,17]. Such an evaluation is mainly

based on the results of the chemical analyses for collected, representative, and reasonably spatially distributed water samples in the area under consideration. The development, design, and application of different concepts, methods, approaches, and methodologies have evolved and continued, such that they are unable to be counted. Some require special skills and capabilities when performed or interpreted; others imply significant uncertainties [18–22]. Moreover, recently, spatial interpolation maps based on kriging and inverse distance weighted (IDW) interpolation methods have been readily applied [23–25]. Although excellent visual representations are reproduced for specific constituents, the heterogeneities, specific outliers, and abrupt changes are not identified due to the averaging and filtering algorithms employed.

There is no single best method to be followed; instead, myriad methods are coupled and integrated as per the study intentions. This work aims to evaluate the practicality of a series of representations, exploring the possibility of improving data representation and initial data analysis to ease the systematic interpretation of generic GW chemical datasets, keeping in mind the newcomers who may not be experts in managing such data. Hence, visualization-based, facile, readily readable, and interpretable curves were tuned and applied to delineate some interconnected controlling factors in Ad-Dawadmi, Kingdom of Saudi Arabia (KSA), as the application case study area. Furthermore, different interpolation algorithms were tested, compared, and discussed, with respect to those that are widely applied, to highlight such variabilities. The classical methods of interpretation have a common shortcoming, that is, their limited spatial representation ability. Thus, a truncation approach was adapted and applied to help contrast the variabilities among different sections of the study area. Finally, the concluded pieces of information were compared to that obtained from the classical widely accepted relationship, i.e., the Gibbs diagram [26].

Location and Study Area Description

Ad-Dawadmi Governorate is located in the northwest of the Riyadh province, on top of Najd hill, the central area of KSA. It is about 330 km west of the center of Riyadh (latitude 24°39.7′ N and longitude 44°23′ E) [27]. It occupies approximately 27,500 km^2, and it ranks 5th among the governorates of the region, having a population of 217,305, according to the 2010 population survey statistics [28]. Most of its lands are located within the scope of the so-called Arabian Shield. The highest rocky elevation in Ad-Dawadmi Governorate is 1307 m in Jabal Al-Nir in the far west, and its lowest plain height is 660 m in the far northeast. The province's surface is generally extroverted, having an average elevation of about 940 m above mean sea level (AMSL). The detailed morphological surface elevation distribution extracted from the DEM raster map is illustrated in Figure 1. As shown, the surface generally slopes towards the east and northeast. Ad-Dawadmi is famous for growing various crops and witnessing remarkable agricultural development in the past thirty years, and it is still fortunate to maintain its production levels [29]. In addition, livestock farming (mainly camels, goats, and sheep), poultry farms, and aquaculture are widely spread all over the governorate.

The thickness of the shallow sedimentary layer ranges between 1.0 and 7.0 m, overlying the rock bed, which slopes from the west to the east [30]. The governorate lies at the extreme east-central border of the Arabian Shield with unconformably overlying Palaeozoic sediments in the central KSA high pediment, which contain Precambrian granitic rock complexes coupled to two belts of folded metasediments and two oval layered basic complexes [31]. These metasediments comprise sulfide and silver mineralizations positioned in parts of an extensive fracture belt trending N–S across the territory. The conformable arenaceous, calcareous Ar-Ridaniyah, and the semipelitic Abt. Formations, are the oldest rocks deposited in a transgressive subsiding, likely marine, environment, during the Precambrian [31,32]. The climate in Ad-Dawadmi is generally hyper-arid with minimal precipitation. The long-term yearly average rainfall was only 4.9 mm during the

ten years from 2005 to 2015 [33]. This year (2022) is the fifth consecutive year having nearly no precipitation except for short showers.

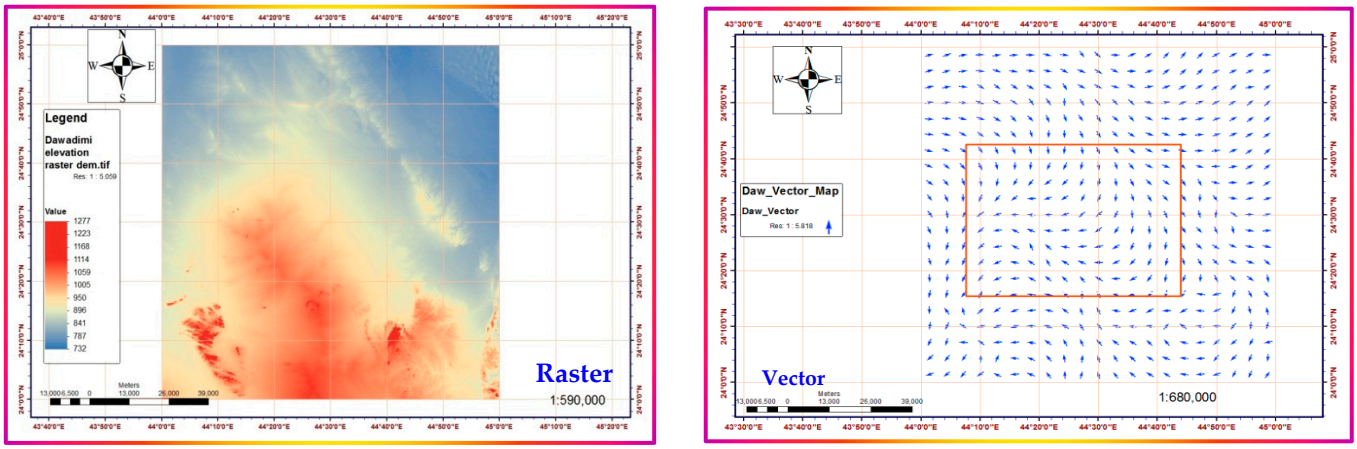

Figure 1. Detailed morphological surface elevation distribution of the Ad-Dawadmi region.

GW is the unique water source for all activities in the study region since precipitation is very limited in duration [27]. However, characterization, monitoring, and studies of the cause-and-effect relationships for the GW in the region are scarce and even absent. The study area considered is the central part of the governorate, namely the Ad-Dawadmi metropolitan area, and its near environs bounded between latitudes 24°18′ to 24°42′ N and longitudes 44°9′ to 44°35′ E. The water table levels were consistently in the range of a few meters, i.e., 2–3 m, and were even further below ground level (BGL) in 1996 [30]. These levels declined sharply and are consistently more than 12 m BGL. The asymptotic spatial distribution interpolated piezometric levels map is given in Figure 2.

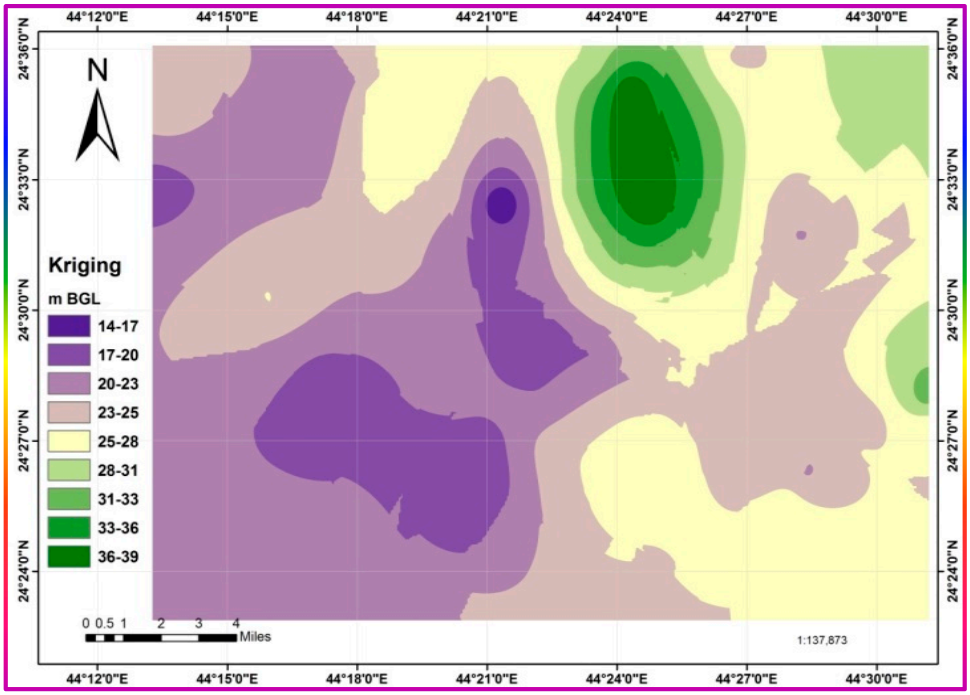

Figure 2. The asymptotic spatial distribution of interpolated piezometric levels map.

2. Materials and Methods

The sampling methodologies, analytical procedures, and instrumental techniques used in the different phases of this work to fulfill the targeted objectives are delineated herein.

2.1. Sampling and Preservation Methodologies

Many sampling campaigns have been conducted to collect GW samples from accessible and active wells covering the study area. Forty-seven GW samples were collected from the study area after enough pumping to ensure that representative aquifer water was attained, and thus reflected the chemistry of the GW with the least possible uncertainty [1]. Acid-cleaned polypropylene bottles were carefully rinsed several times with the well water before sampling, then filled, preserved, and cooled as per rules for different analyses. The respective precautions and rules were considered, along with the commensurate care, preservation, immediate pretreatments, and in-field measurements. The areal distribution of the sampling points is shown in Figure 3. One-liter polypropylene bottles were collected for the hydrochemical analyses (major cations and anions), cooled without adding a specific preservative agent, split, and pretreated following the rules of different individual analyses according to the standard methods and sampling directions [34–36]. Samples of 1 L for ammonium and nitrate ions analysis were acidified with ≈2 mL concentrated trace element analysis-grade sulfuric acid. Samples were chilled in an icebox until they were taken to the laboratory within 6–8 h of sample collection. All analyses were carried out in the Water and Environment Research Unit (WERU), college of Science and Humanities, at Ad-Dawadmi, Shaqra University.

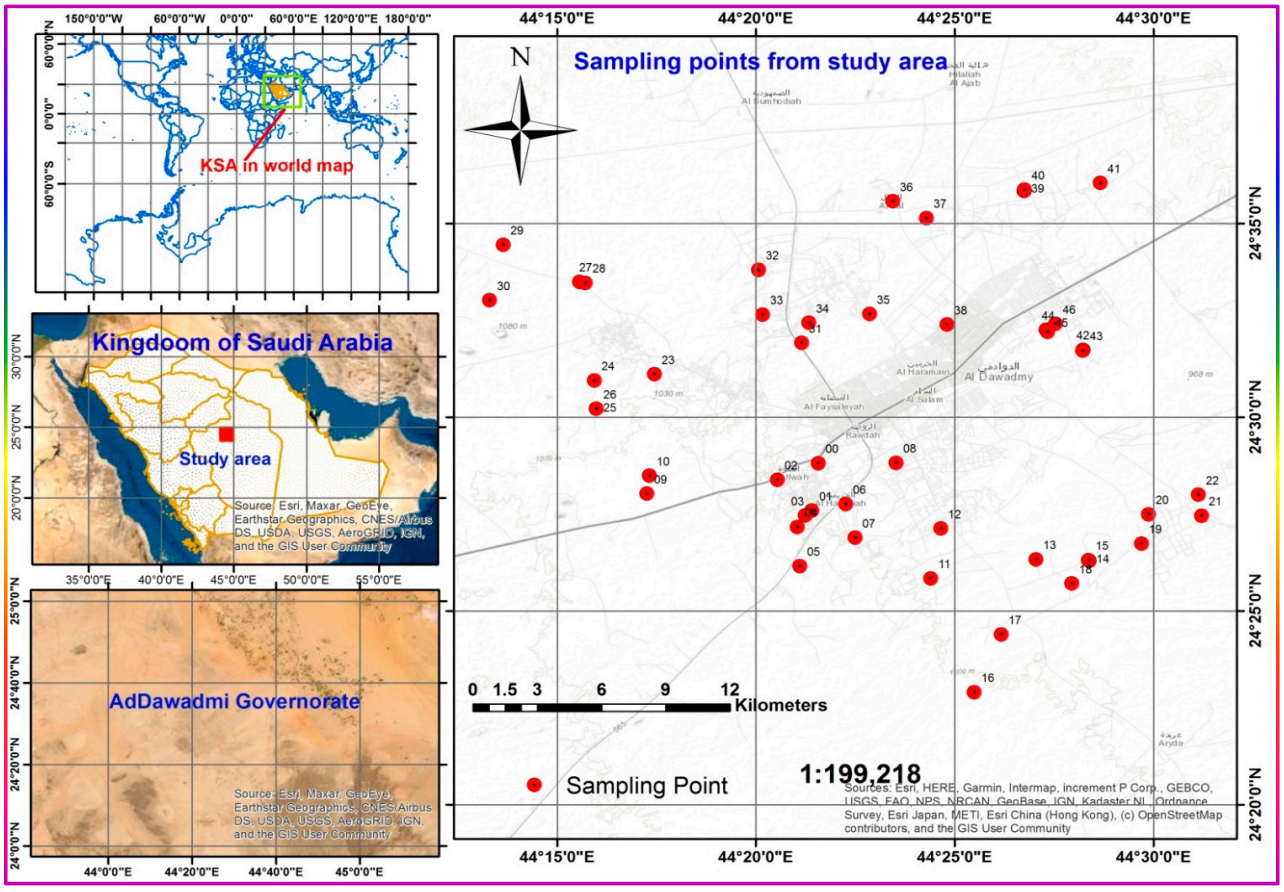

Figure 3. Study area location and sampling point distribution.

2.2. Analyses Techniques, Methodologies and Procedures

a. In-Field Parameters

Electrical conductivity (EC) is a measure of the ability of water to carry an electrical current, and depends on the salt content of water. The EC of water samples was measured using an electrical conductivity meter (ThermoScientific, ORION STAR A122, Waltham, MA, USA). The meter was calibrated before going into the field, with occasional operational

checks during the sampling campaign at random intervals using the calibration solutions closer to the salinity levels. The hydrogen ion concentration (pH) was recorded in the field using a pH sensing electrode (PascoScientific pH electrode, Roseville, CA, USA) connected to a data logger (Explorer GLX, Pasco, Roseville, CA, USA) via PASPort CHEMISTRY Sensor, PascoScientific. The temperature (T, °C) was measured using an independent electrode connected to the data logger via the Passport CHEMISTRY Sensor. The pH meter was calibrated on the day immediately before the sampling campaign. Dissolved oxygen levels (DO) in mg/L were measured using a Pasco Scientific DISSOLVED OXYGEN meter connected to the same data logger used to record pH and temperature. The DO electrode was calibrated on the day before sampling using a zero-oxygen solution prepared by dissolving a large-enough amount of sodium sulfite (Na_2SO_3) in distilled water. In contrast, the saturated solution was prepared by continuous aeration of 300 mL of distilled water for half an hour. Calibration practices, electrode storage, and maintenance were undertaken following the manufacturer's instructions for each electrode.

b. Hydrochemical Analyses

Careful preparation, assembly, and adjustment of the experimental installations and conditions, checking of the instruments, and preparation of the standards and starting materials are of utmost importance to provide acceptable and reliable analysis results. Method validation evaluates whether the precision and accuracy obtained by following the procedure are appropriate for the problem (i.e., results are fit-for-purpose). The current work followed the validated procedures stated in the Standard Methods for the Examination of Water and Wastewater (2017) [37]. The standard methods resulted in excellent validation practices and contained, in some cases, numerous stages to remove interferences and ensure the reliability of the results obtained. These precautions and preparatory steps may be deemed beneficial as they are commensurate with the study intentions, confidence levels, and accuracy required. When such aids or modifications were adopted, the rule of thumb, namely, that they must not compromise the analysis reliability, was ensured by applying quality control, operational checks, and quality assurance practices.

Bicarbonate (HCO_3^-) was determined titrimetrically against sulfuric acid by modified neutralization procedure No. 2320B [38]. Samples used for HCO_3^- received no prior treatments, except being kept out of contact with air. A minor modification adopted was the use of Phenolphthalein (1%) and Methyl orange (0.01%), and titration until a constant pH of 4.3, ensured with a pH meter, was achieved. Chloride (Cl^-) was determined volumetrically by titration against silver nitrate (ergonometric titration, procedure No.4500- B Cl^-) using potassium chromate. The procedure steps and calculations were followed thoroughly. Calcium (Ca^{2+}) and magnesium (Mg^{2+}) were determined titrimetrically against (Na_2EDTA) by a complexometric method [38]. Sodium (Na^+) and potassium (K^+) concentrations were quantified using a flame photometer (MICROPROCESSOR FlamePhotometer, Model-1382) following procedures No.3500-Na B and 3500-K B.

Sulfate (SO_4^{2-}) ion concentration was determined following the turbidity method (procedure No.4500-SO_4^{2-} E) using a spectrophotometer (JENWAY 6850 UV/Vis. Spectrophotometer) at a 420 nm wavelength. Calibration curves ensured the linear relationship between absorbance and concentration, with R^2 consistently higher than 0.99. Nitrate (NO_3^-) ion concentration was measured using a relatively facile, modified method using phenol sulfonic acid as a complexing agent at a 410 nm wavelength [39]. Ammonium (NH_4^+) ion concentration was determined using the modified ammonia diffusion method [40]. This method is based on converting dissolved ammonium ions to ammonia gas, increasing the pH value using sodium hydroxide solution, and collecting the stripped ammonia gas in an acid cap containing 5 mL of 0.05 N H_2SO_4. After incubating the samples for five days at room temperature and shaking at an amplitude of 180 rpm, the contents of the acid caps were washed and diluted to 100 mL. Nessler's reagent was then added to a small portion of these samples, and the intensity of the resulting yellow color was measured spectrophotometrically at a 405 nm wavelength.

2.3. Geospatial and Geostatistical Analyses

The spatial analysis tools of ArcGIS 10.8 software were used to analyze the spatial variation in the GW chemical and physical parameters. Many interpolation algorithms are built into the ArcGIS framework. Interpolation is a statistical method by which corresponding known values are used to estimate an unknown, or is simply the method of obtaining values at positions between the data points [41,42]. Simple kriging and inverse distance weighted (IDW) algorithms have been widely used to generate a complete surface map using data points at sampling locations. Each approach has its own algorithms, but both yield an averaged and smoothed distribution of variables that may mask the localized extremes. In this study, the natural neighbor and trending interpolation methods were compared to IDW and kriging to determine which is more suitable for identifying the heterogeneities and extremes in the datasets.

3. Results and Discussion

3.1. Physicochemical Properties

The descriptive statistics summary of the physicochemical properties and field pieces of information of the sampled wells is given in Table 1. The temperatures ranged from 21.5 to 31.8 °C, with an average of 27.32 °C and standard deviation (SD) of ±2.168, n = 47. Ahmad et al. pointed out that the temperature variabilities are related to the recharge with rainfall, and that deeper GW has a higher temperature than shallow GW [43]. In the bubble diagram, three parameters can be related in the XY plane, with X and Y each representing one parameter, and the normalized radii of the bubbles representing the third. The sampling point ID can also be shown. The temperature plot against EC with the radii of the bubbles representing the well depth and water table levels is given in Figure 4. It shows no obvious relation, but the semi-horizontal trending line confirms a slight direct trending theme between temperature and EC. Moreover, this trend seems independent on both well depth and the water levels, with only a slightly inverse dependence of EC on well depth. This behavior indicates that rainfall recharge may not be dominant, and that another source affects the system.

pH coupled to temperature dominantly controls dissolution, precipitation, mass transfer, and all other related GW system processes. Measurement of GW pH provides essential information about the geochemical equilibrium [44,45]. The relationship between pH and EC, coupled with calcium, magnesium, bicarbonate, and sulfate ion concentrations as the bubble radii, are shown in Figure 5. The pH values varied from 6.8 to 8.35 with an average of 7.332 ± 0.345 SD, n = 47, showing that pH values dominantly lie in the neutral to slightly alkaline range. This theme emphasizes the inverse relationship between EC and pH, with a congruent decrease in calcium and sulfate ion concentrations. This behavior highlights the precipitation and removal of calcium at higher pH values. The individual differences between Ca^{2+} and SO_4^{2-} may be ascribed to differences in solution activities concerning each constituent. Another principal contributor to such an effect is the HCO_3^- concentration, which exhibits the same trend with Ca^{2+} as SO_4^{2-}; Figure 6. Mg^{2+} concentrations were consistently lower than Ca^{2+} ion loads, except for one sample showing a Mg^{2+} load that was extremely higher than that of Ca^{2+}. Mg^{2+} showed a smoother trend with pH and had no definite trend with HCO_3^- and SO_4^{2-}, as was the case with Ca^{2+}.

Another apparent and exciting trend is the negative variation of Ca^{2+} with the temperature (Figure 7), which corroborates the occurrence of calcium salt precipitation. Calcium salts' solubility, and especially that of sulfates, is inversely proportional to temperature. The less-hydrated forms, hemihydrate (bassanite $CaSO_4 \cdot 0.5H_2O$) and anhydrite ($CaSO_4$), were found to be strongly affected by temperature increase and concentration of coexisting ions, which may reduce the activities of precipitants [46–49]. Increasing concentrations of co-occurring ions reduce the activities of potential precipitant ions (i.e., Ca^{2+}, HCO_3^-, and SO_4^{2-}), which may propagate a large share of calcium, magnesium, sulfate, and bicarbonate ions at higher EC values, leading to processes of aggressive salinization. Moreover, these themes highlight a significant tendency for scale formation when GW is used at

elevated temperatures. The temperature in the study area approaches 50 °C on hot summer days, which may affect GW for domestic uses.

Table 1. Summary of descriptive statistics of the collected data of the GW samples.

Variable	Mean	SE Mean	StDev	Minimum	Q1	Median	Q3	Maximum	Range	IQR	Anderson–Darling Normality Test	
											p-Value	Decision
Temp. (°C)	27.321	0.316	2.168	21.5	25	27.5	29	31.8	10.3	4	0.011	fail
pH	7.3372	0.0504	0.3454	6.8	7.1	7.33	7.54	8.35	1.55	0.44	0.321	pass
EC, microS/cm	5227	546	3745	255	2939	4280	7050	17990	17735	4111	<0.005	fail
TDS (ppm)	3293	344	2359	161	1852	2696	4442	11334	11173	2590	<0.005	fail
Na (epm)	28.77	3.68	25.22	0.47	11.3	21.91	34.83	103.48	103.01	23.53	<0.005	fail
K (epm)	0.1694	0.0145	0.0991	0.04	0.1	0.15	0.22	0.5	0.46	0.12	<0.005	fail
Ca (epm)	25.9	2.74	18.81	2.09	11.47	21.69	34.93	83.41	81.32	23.46	<0.005	fail
Mg (epm)	7	1.26	8.62	0.04	1.89	5.04	10.5	55.65	55.61	8.61	<0.005	fail
NH4 (epm)	0.0006	0.0004	0.002	0	0	0	0	0.01	0.01	0	<0.005	fail
TC (epm)	61.84	6.58	45.09	3.02	29.42	51.71	91.74	208.39	205.37	62.32	<0.005	fail
HCO_3 (epm)	5.162	0.246	1.685	2.11	3.97	4.96	6.14	8.79	6.68	2.17	0.474	pass
Cl (epm)	29.25	4.22	28.94	0.54	9.67	18.6	42.77	142.92	142.38	33.1	<0.005	fail
SO_4 (epm)	27.14	2.52	17.29	0.26	13.43	24.22	41.25	69.21	68.95	27.82	0.072	pass
NO_3 (epm)	1.172	0.159	1.092	0	0.47	0.83	1.88	4.34	4.34	1.41	<0.005	fail
TA (epm)	62.72	6.3	43.21	3.49	33.06	52.82	84.03	196.01	192.52	50.97	<0.005	fail
Alt. (m AMSL)	976.23	4.17	28.6	911	947	985	996	1034	123	49	0.007	fail
Well Depth (m BGL)	38.43	1.21	8.28	25	30	40	45	52	27	15	<0.005	fail
Water table (m BGL)	23.979	0.77	5.277	12	20	25	26	40	28	6	<0.005	fail
Discharge, m^3/day	37.77	2.31	15.84	15	30	40	40	80	65	10	<0.005	fail

ppm: parts per million, epm: equivalents per million, AMSL: above mean sea level, BGL: below ground level.

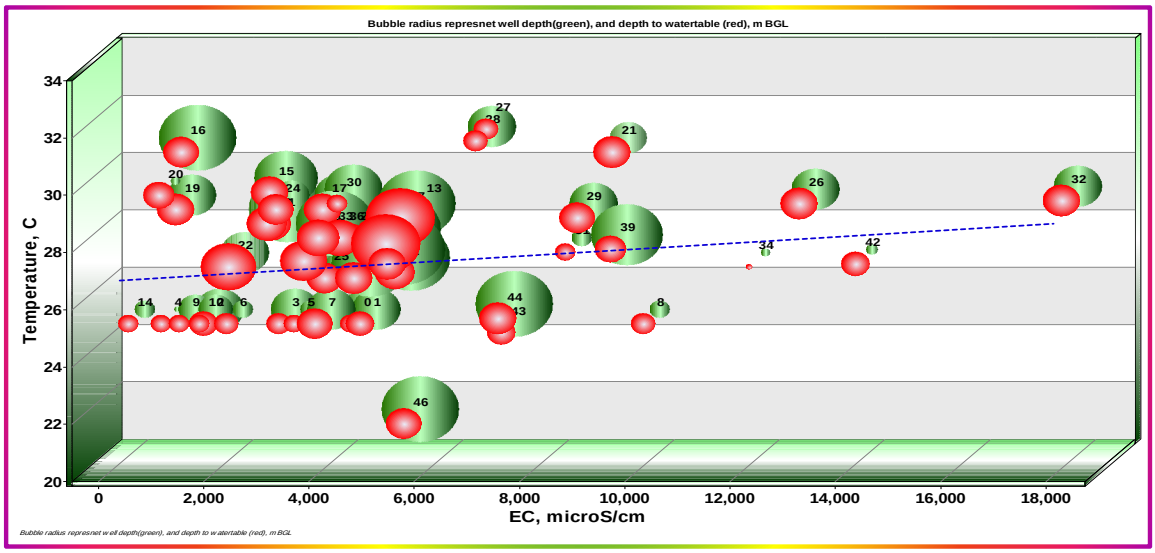

Figure 4. Dependency of EC on temperature, well depth, and the water table depth. Bubble radii represent normalized well depth (green) and the water table depth (red).

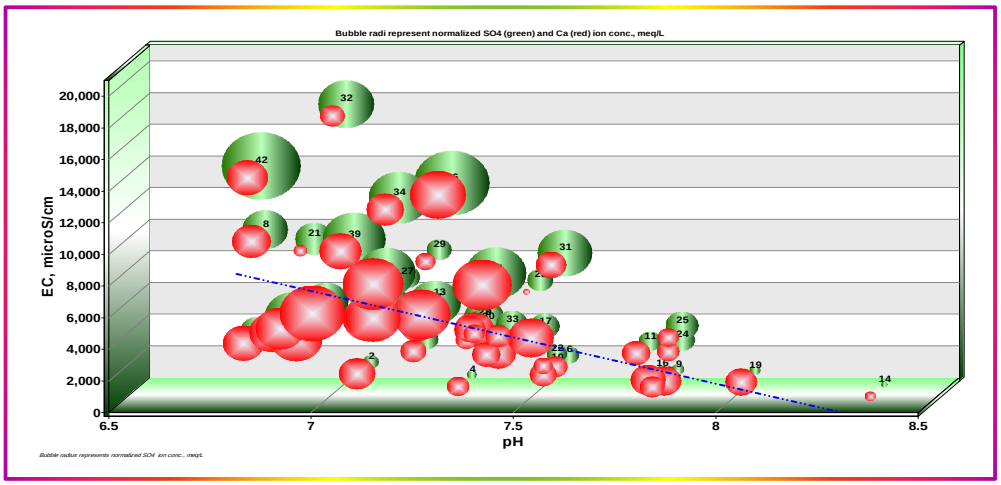

Figure 5. Dependence of EC on pH and sulfate and calcium ion concentrations. Bubble radii represent normalized SO_4^{2-} (green) and Ca^{2+} (red).

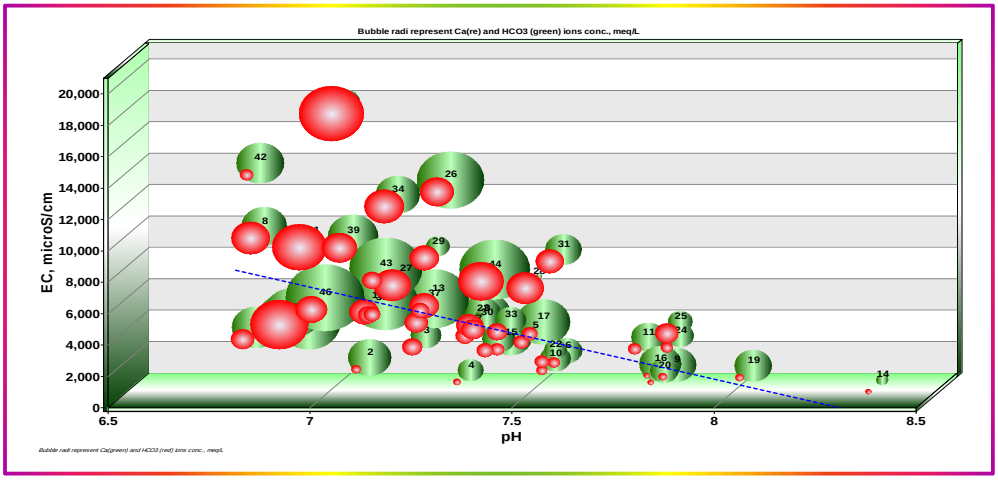

Figure 6. Dependence of EC on pH and calcium and bicarbonate ions concentrations. Bubble radii represent normalized HCO_3^- (green) and Ca^{2+} (red).

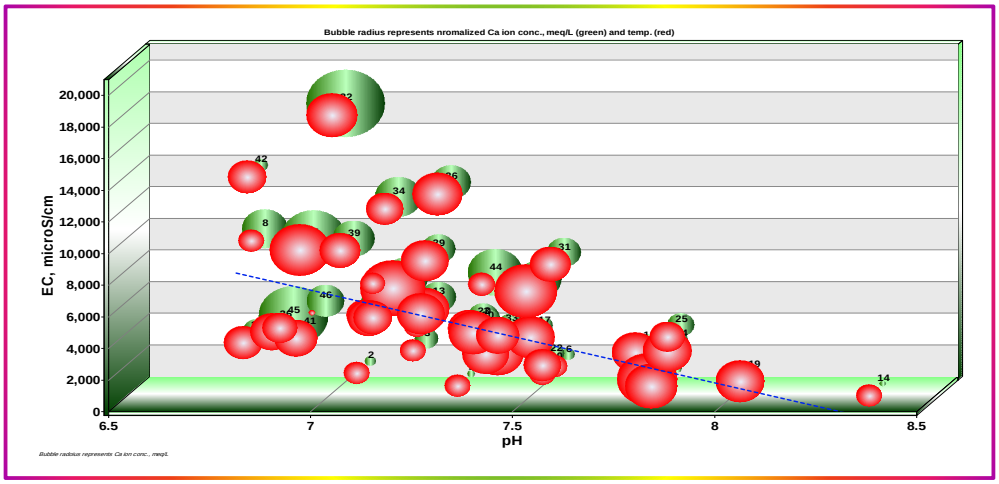

Figure 7. Dependence of EC on pH and Temp., and calcium ion concentrations. Bubble radii represent normalized Ca^{2+} (green) and Temp. (red).

3.2. TDS Spatial Distribution Maps

Total dissolved solids (TDS) is a collective term used to describe the total content in the water sample of the major cations (Na^+, K^+, NH_4^+, Ca^{2+}, and Mg^{2+}) and major anions (HCO_3^-, CO_3^{2-}, Cl^-, NO_3^- and SO_4^{2-}). Usually, it is calculated asymptotically from the measured EC by applying, almost arbitrarily, a response factor in the range of 0.5 to 0.65, according to the type of water and EC range. The EC ranged from 255 to 17,990 µS/cm with an average of 5227 µS/cm and SD of ±3745, n = 47. The calculated TDS values ranged from 161 to 11,334 mg/L, with an average of 3293 mg/L and SD of ±2359, n = 47. Large SD values denote the significant variability within the area, with no dominant TDS or EC range; this may be due to localized influencing parameters, such as point sources, rather than effects of lithology, catchment-wise, or basin-wise processes. Classification of GW and its suitability for different purposes is mainly dependent on EC or TDS, but this is beyond the scope of the current demonstration, which focuses mainly on identifying the major interconnected factors and sources controlling the aquifer geochemistry. The areal distribution of EC in the study area using different interpolation algorithms is shown in Figure 8.

Each interpolation method yielded a somewhat different pattern. IDW and natural neighbor (NN) algorithms retain the relative view of the variability among individual sites. Kriging interpolation provided a more smoothed averaging over the entire area, although it still partially retained the view of individual heterogeneities. The trending interpolation algorithm yielded an aggressively smoothed distribution of EC without highlighting any intra-area heterogeneity, indicating that salinity or electrical conductivity increases from south to north. However, a possible conclusion is that, regardless of the algorithm applied, except for the trending interpolation method, localized variabilities are remarkable, and have a generally increasing trend in EC from south to north and northeast, as shown in the general morphology in Figure 1. Moreover, pockets of higher EC values are highlighted within each subgroup of the EC level, indicating the effects of point source activities, primarily agriculture and livestock farming.

ECs are strongly dependent on the weather, rainfall durations and amounts, the host rock, and the residence time [50]. Thus, the hyper-aridity of the study area with deficient precipitation and high evaporation may adversely affect the GW salinity levels. Furthermore, human activities such as agricultural practices, including fertilizer application (relatively limited in the current case study) and irrigation using high-EC GW, coupled with high evapotranspiration, may lead to concentrating salts in the soil, which may be washed out to the aquifer with the subsequent irrigation cycle or rainfall event. Given the uneven distribution of farms, the appearance of EC (salinity) pockets, especially within or near agricultural farms, seems to reasonably be a result of the salinization mechanism mentioned above. This trend agrees with Ahmad et al. in their evaluation of GW in the state of Qatar [43]. Moreover, the general trend of increasing salinity from south to north and northeast may be ascribed to the migration of high-salinity water (the most upper layer of recharging water) from south to north following the general morphometric trend (Figure 1). In addition, the mixing of deep water (brackish) cannot be excluded since the depths of the wells in the northern part of the study area are greater.

Coupling higher well depths with lower altitudes may support reaching a deeper water layer that may be of originally higher salinity. To validate this hypothesis, the depths of the wells were normalized to the mean sea level and correlated against EC levels; Figure 9. Inspecting Figure 9 indicates no relation between EC levels and normalized well depths, with extremes lying everywhere, such as IDs 39, 42, and 32, in different localities and at different normalized depths. This theme may nullify the hypothesis of deep layer water mixing and corroborates the dominance of the point source's effects.

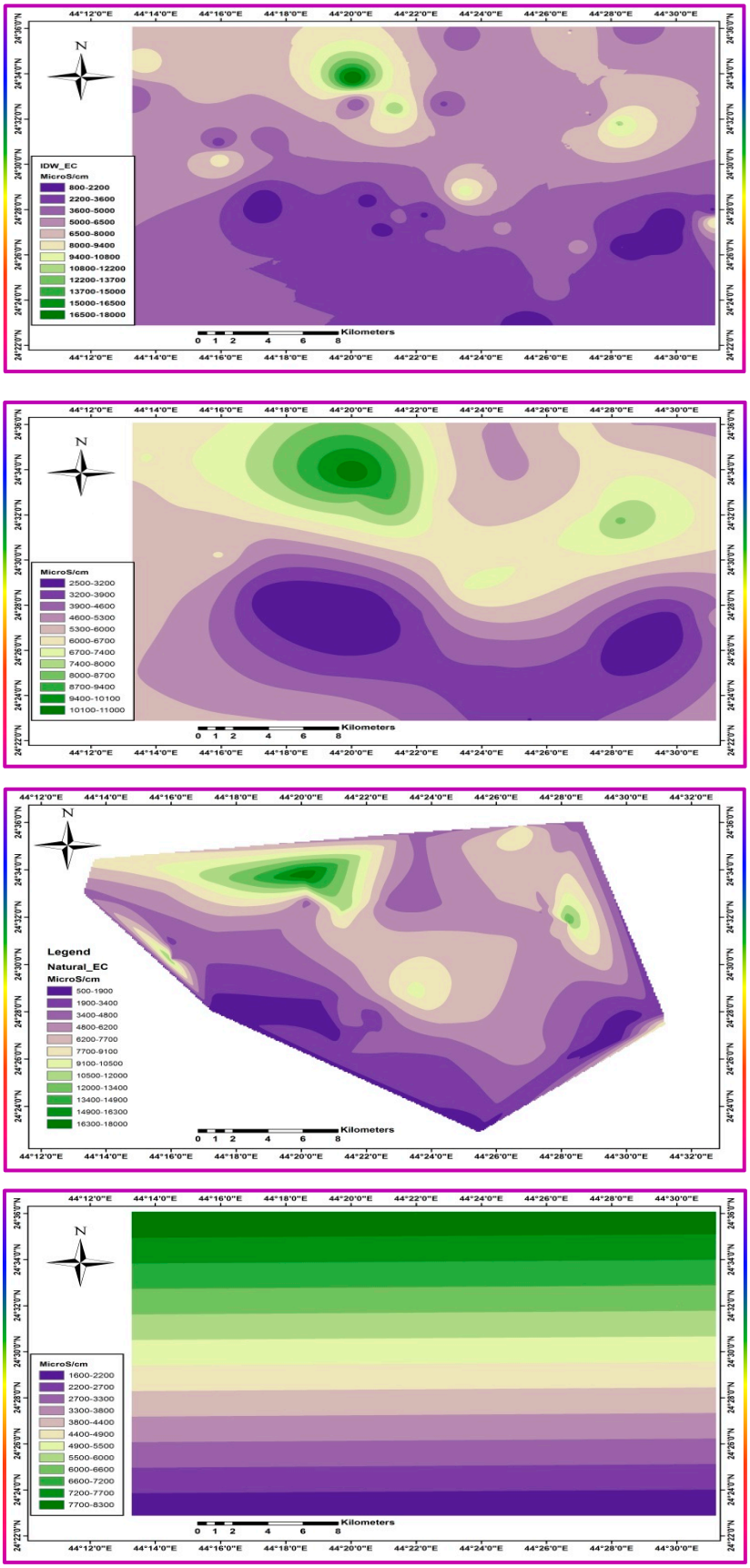

Figure 8. The areal distribution of EC in the study area using different interpolation algorithms. IDW, kriging, natural neighbor, and trending, from the top down.

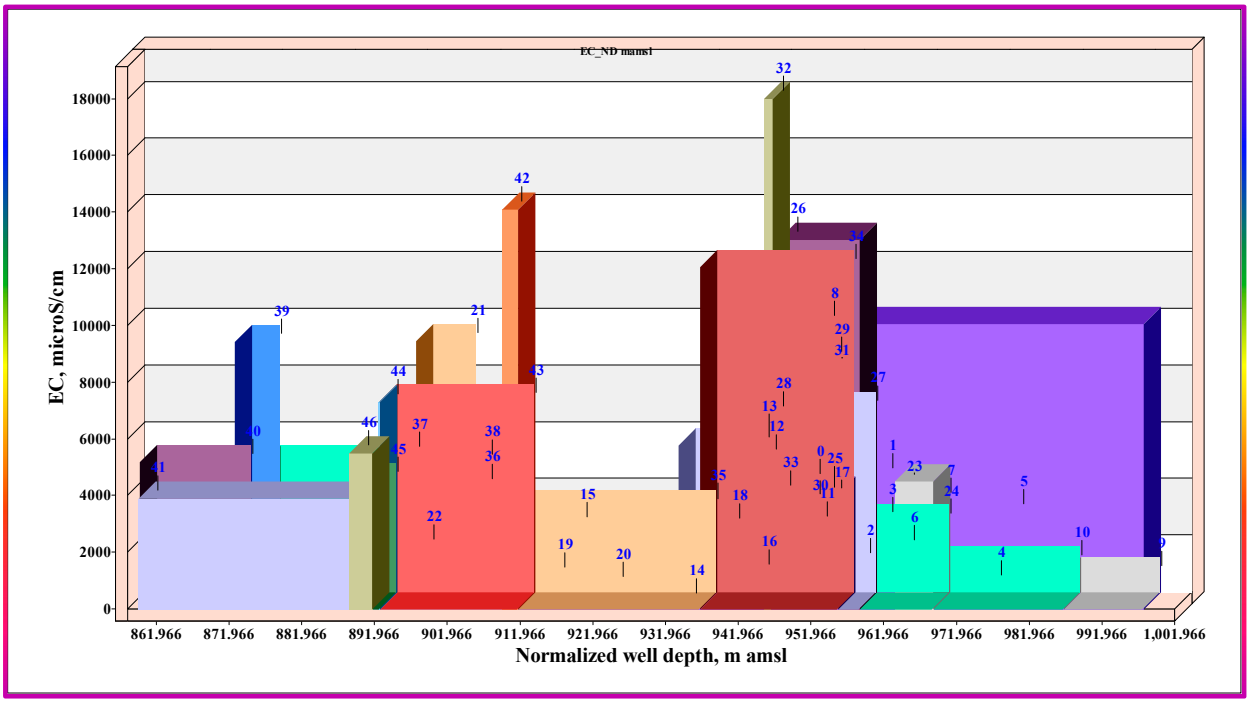

Figure 9. Correlation of the depths of the wells normalized to the mean sea level against EC levels.

3.3. Major Ions Constituents'

The distribution of major ion constituents provides information about the origin, history, and physicochemical, hydrogeochemical, and biogeochemical processes [51–55]. Prominent differences were observed among the total and individual components all over the study area. The study area can be sliced into parts: the northern half, the southern half, the western half, the eastern half, the northwestern part, and the southwestern and southeastern parts. Stiff diagrams were used to demonstrate averaged variabilities of the major constituents in each section. Figure 10 shows the averaged spatial distribution of major ions (anions and cations) using Stiff diagrams, with the central polygon representing the average over the whole study area. All Stiff diagrams were drawn with the same unit (epm) and scale to enable quick comparison and identification of the variabilities according to the size and polygon geometry.

Figure 10 shows notable variations among the individual constituents increasing from south to north and west to east. This trend was not prominent in total load only, and it appears clearly in the changes in the relative proportions of the major constituents. Average water types can be concluded from such diagrams as follows, expressed in terms of the most dominant two cations and two anions, respectively:

- The study area (all samples): $Na^+ - Ca^{2+} // Cl^- - SO_4^{2-}$
- The northeastern part: $Na^+ - Ca^{2+} // SO_4^{2-} - Cl^-$
- The northwestern part (Masddah): $Ca^{2+} - Na^+ // Cl^- - SO_4^{2-}$
- The southeastern part (Addasmah and AsSmearah): $Ca^{2+} - Na^+ // Cl^- - SO_4^{2-}$
- The southwestern part: $Ca^{2+} - Na^+ // SO_4^{2-} - Cl^-$
- The eastern half: $Na^+ - Ca^{2+} // SO_4^{2-} - Cl^-$
- The western half: $Na^+ - Ca^{2+} // Cl^- - SO_4^{2-}$
- The Northern half: $Na^+ - Ca^{2+} // SO_4^{2-} - Cl^-$
- The southern half: $Na^+ - Ca^{2+} // Cl^- - SO_4^{2-}$

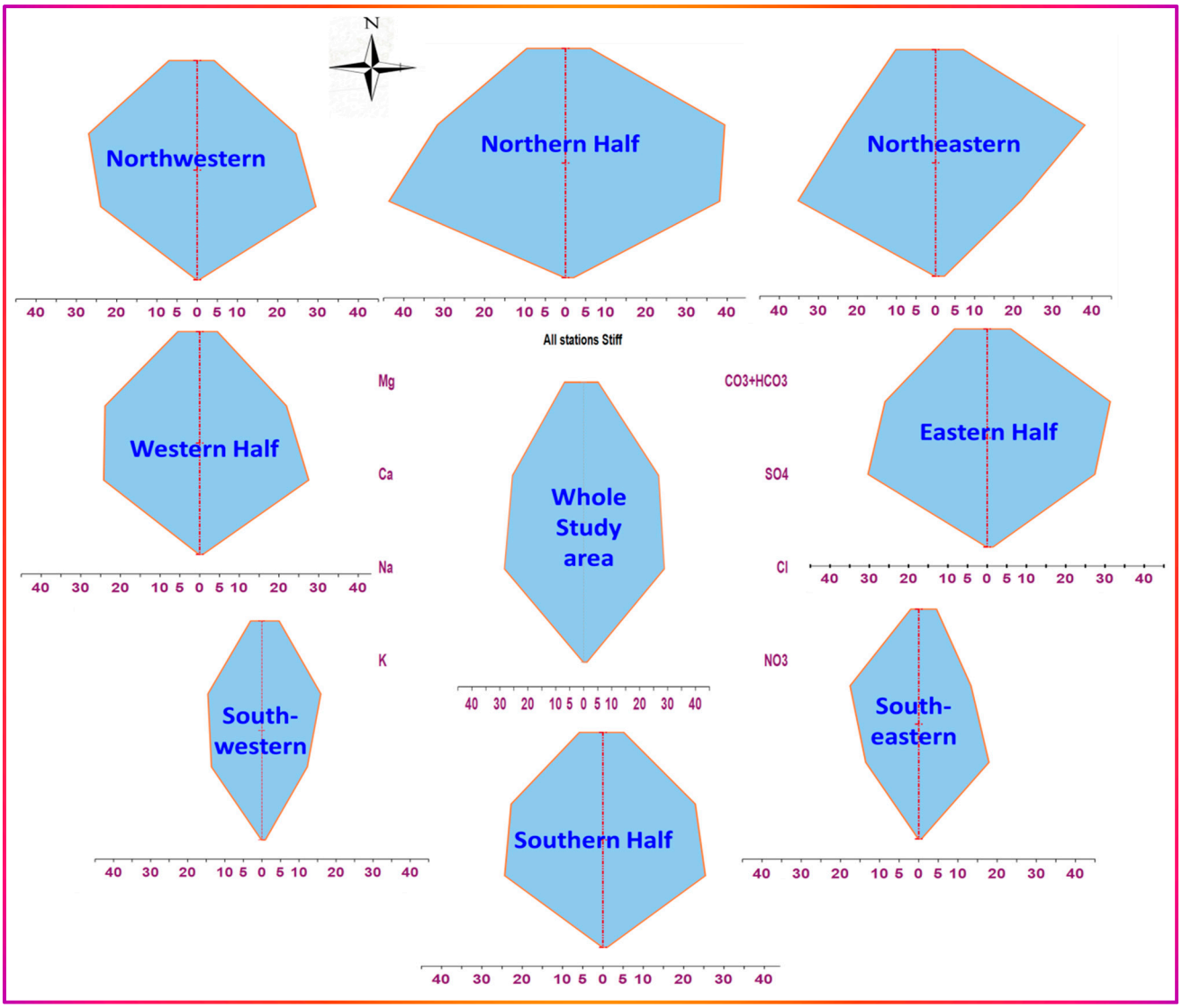

Figure 10. Stiff diagrams of averaged major constituents' distribution throughout selected partitions of the study area.

Although the water types are not diverse, with only minor observed variabilities, the differences in the proportions of the individual and total loads are evident among the different halves, and even among the parts within the same half. The potential sources of solutes may be: (a) rainwater usually occurs in the form of showers following dust storms heavily loaded with aerosols that might dissolve readily in rainwater and rock–water interactions; (b) anthropogenic sources include fertilizers, livestock manure, underground sewers, tank seepages, landfills' leachate, and septic ponds in unsewered localities; (c) the water–rock interactions may differ slightly across the whole area, with variations concerning the flow path and residence time from one locality to another. Some localities may demonstrate receiving more rock-weathered salts and leachates in the morphological downward direction, such as the north and northeastern parts.

The occurrence of local or even point source processes contributes to higher salinities. The activities were not observed to be different across the area, nor due to the presence of point sources in the northern half, but they were older than those in the southern part, which partly explains the appearance of more concentrated salts in the northern part. Furthermore, as shown in Figure 11, sodium ion concentrations were consistently greater than those of calcium, suggesting the occurrence of direct cation exchange, releasing Na^+

from the clay matrix and binding Ca^{2+} instead. A dynamic equilibrium state may be attained between calcium and sodium ions due to the presence of large amounts of Ca^{2+} and Na^{+} ions, especially at high salinity levels, which may interfere with and even reverse the exchange affinity of clay for both ions within the domain- and time-scale frames of clay intra-beads. Slight differences between equivalent amounts of sodium and calcium, except in the northern half, support this explanation, which demonstrates a more significant excess of sodium. Sodium salts have far higher, and even unlimited, solubilities than calcium, and are precipitated readily when exceeding the solubility limits.

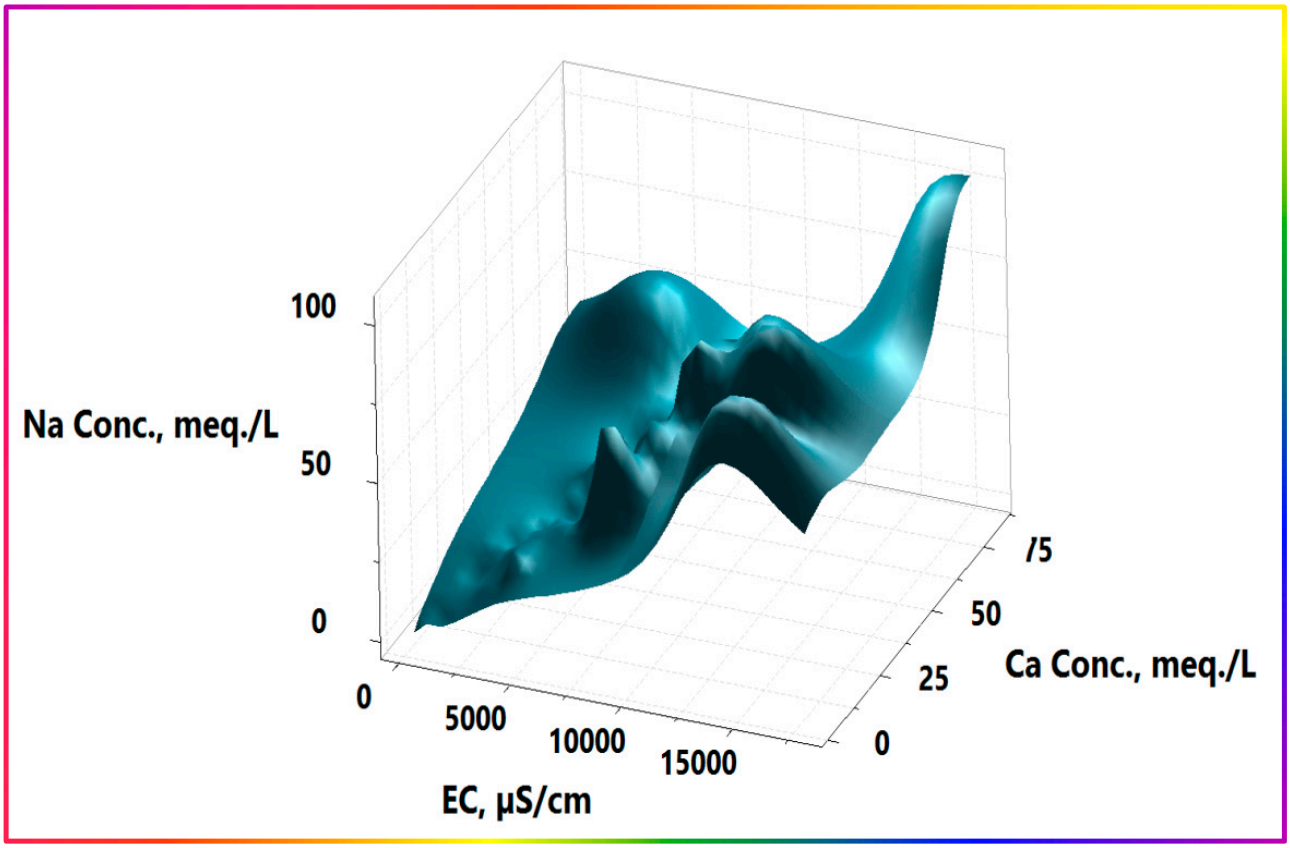

Figure 11. Three-dimensional surface plot of calcium and sodium contributions with EC.

The increase in sulfate ion concentrations (Figure 12c) may suggest precipitation of calcium, mainly in the form of calcium carbonate. Figure 12b,d show that Ca^{2+} and HCO_3^- have an inverse distribution to each other. Continuous HCO_3^- replenishment by absorbing atmospheric carbon dioxide into irrigation water during watering causes calcium precipitation, leading to a final concentrating profile of the other constituents. This hypothesis requires equimolar amounts of chloride to sodium to exclude ion exchange. This equimolar provision is suitable for all parts except the northeastern part, where there are lower chloride concentrations. This anomaly suggests the occurrence of ion exchange due to the availability of calcium rains at lower pH values, of about 6.8, as shown in Figure 12a. Large loads of other soluble ions interfere with calcium salt precipitation by lowering its ion activity [47,49,50].

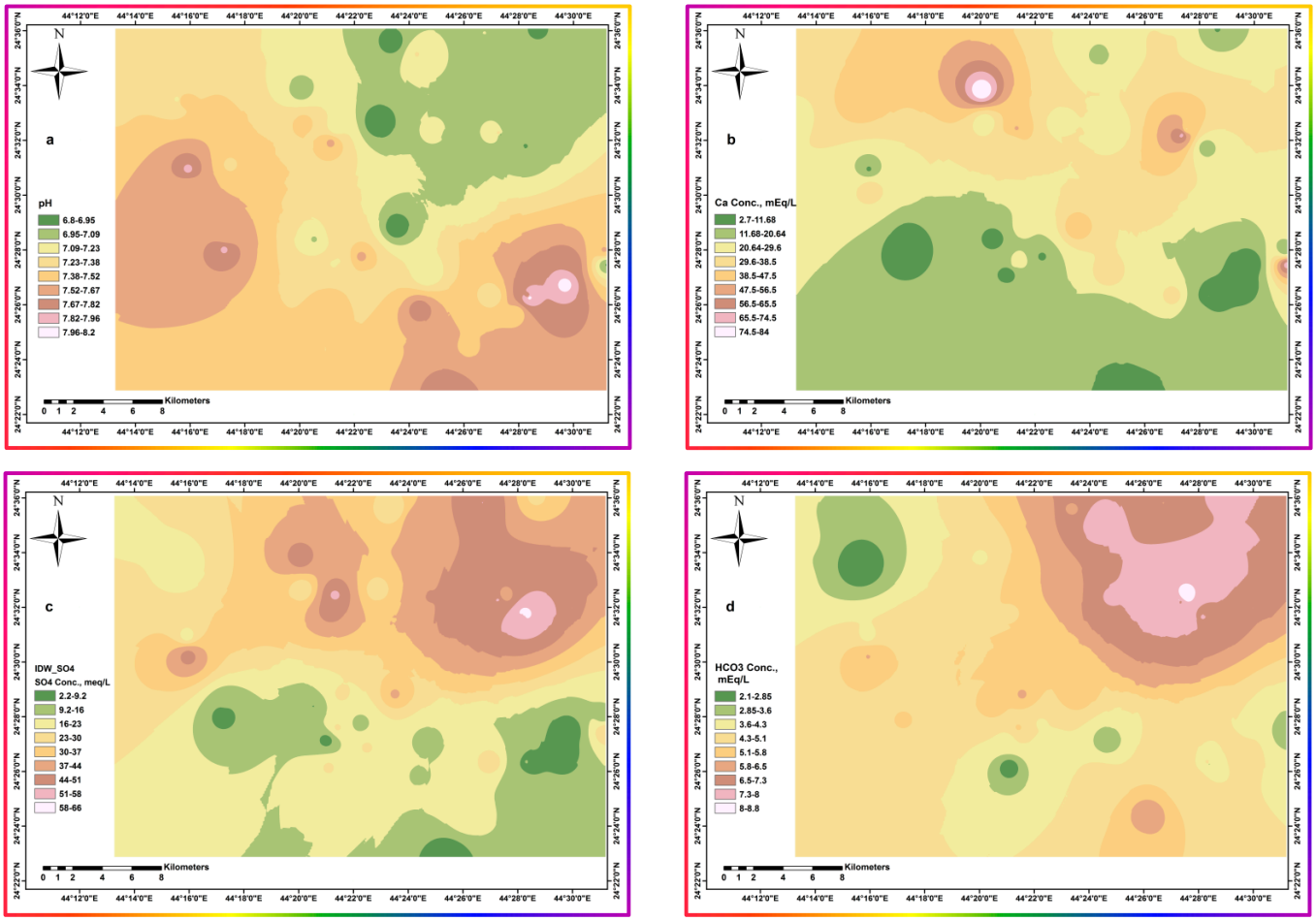

Figure 12. Spatial distribution of different parameters throughout the area. (**a**) pH (**b**) Calcium Conc. (**c**) Sulfate Conc. (**d**) Bicarbonate Conc.

3.4. Interactions and Relationships among the Major Constituents

Figure 13, the scatter box plot matrix, shows the collective interactions and relationships among the four main cations, Na^+, K^+, Mg^{2+}, and Ca^{2+}, and the four main anions HCO_3^-, Cl^-, SO_4^{2-}, and NO_3^-, in addition to pH and EC. Although EC represents the ultimate response parameter for such interactions, it is considered in this plot to be an interconnected parameter used to identify its main contributors. To compare the equimolar changes, all concentrations are expressed in epm (to resemble the ion ratio diagrams). Moreover, individual parameters' histograms are included to visualize the nature of their distribution. In addition, normality testing for individual parameters was executed using the Anderson–Darling method (Table 1), and the decisions (fail or pass) are given and discussed in their respective sections, along with their *p*-values at a 95% confidence level. The Anderson–Darling statistic measures whether a given sample of data is drawn from a given probability distribution. The Anderson–Darling test has a severe flaw when applied to real-world data, since it is severely affected by ties (a tie means the occurrence of identical values more than once in the dataset). In the case under consideration, the dataset is tie free, and hence the Anderson–Darling approach is the test method of choice because it has excellent theoretical properties. The test rejects the hypothesis of normality when the *p*-value is less than or equal to 0.05 [56–58].

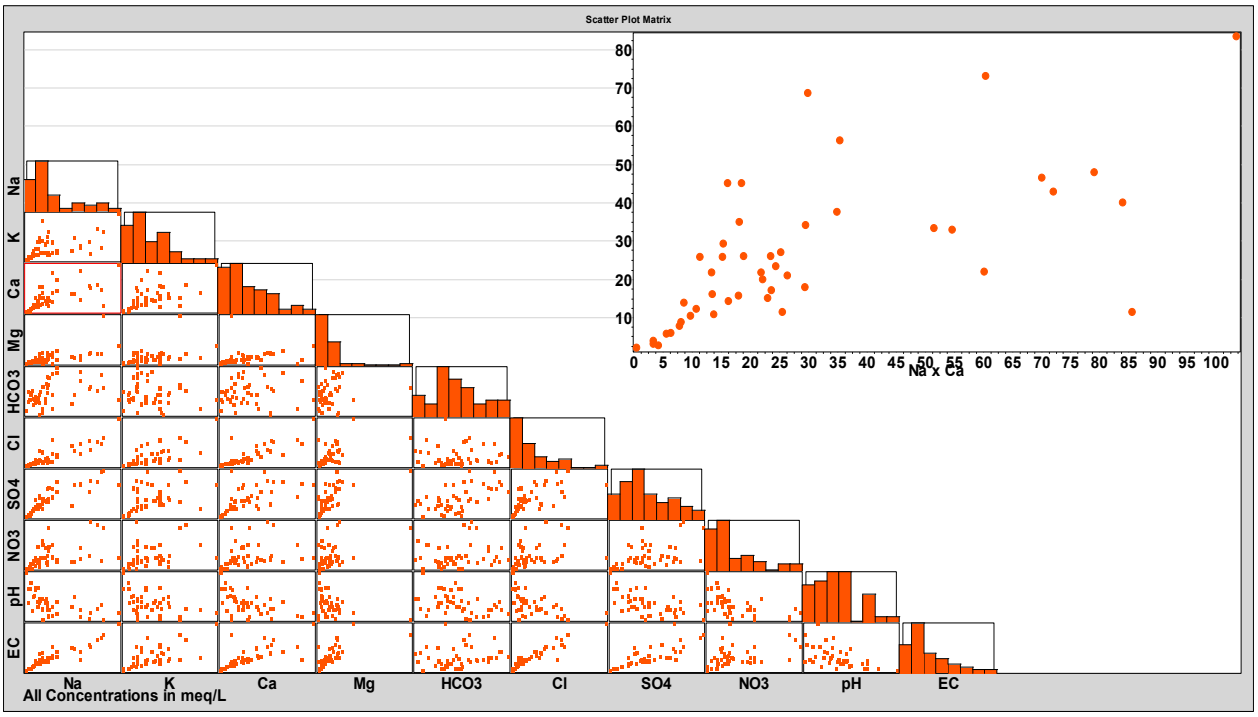

Figure 13. Scatter box plot matrix of the interactions among the major constituents across the study area.

The main merits of the scatter box plot matrix include the overall collective representation of the whole spectrum of major ions in one plot, simplicity of production, representation of extensive datasets in one graph, and direct readability. The following inferences could be drawn from inspecting the scatter box plot matrix:

1. EC values are mostly linearly dependent upon Na^+, Cl^-, Mg^{2+}, Ca^{2+}, and $SO_4{}^{2-}$, especially at lower salinity levels. Ca^{2+} shows a deviation from that linearity at higher levels, which may be ascribed to its precipitation with a similar but milder trend for $SO_4{}^{2-}$. The normality test for EC distribution failed with a p-value < 0.005, which may be caused by localized processes leading to a wide span of EC values with no remarkable central tendency. Moreover, higher EC values were noted for wells in the older and more intense farms. $HCO_3{}^-$, $NO_3{}^-$, and K^+ exhibited no general trend with EC. On the contrary, pH exhibited a generally expected inverse relationship with EC, with remarkable deviation from linearity at higher EC values demarcating the occurrence of concurrent processes that alter EC with a quasi-exponential relationship instead of a linear relationship. One such change may be ascribed to the repeated replenishment with $HCO_3{}^-$ from cycle to cycle of irrigation, since the absorption of atmospheric CO_2 lowers the pH, leading to more dissolution of the contacted soil salts; more dissolution of carbonates again gives rise to higher pH values that result in precipitation of Ca salts, leading to a another lowering in pH. This supposed vicious salinization cycle is illustrated in the simplified Scheme 1, showing a continuous exacerbation of GW salinity. These cycles of pH fluctuations lead to an ultimate rise in EC values by changing the major contributor's proportions.
2. pH has a different theme to EC, as expected. It trends inversely with Ca^{2+} and $SO_4{}^{2-}$ ion concentration, whereas $HCO_3{}^-$ fluctuates sinusoidally as it repeatedly goes up and down. The normality test for pH passed with a p-value of 0.321, as it fluctuates with no ultimate sink or source terms, leading to net accumulation in a particular portion of the system. A 3D surface plot delineating this trend is portrayed in Figure 14a. The plot corroborates the finding of the scatter box plot matrix, namely, that calcium inversely fluctuates with pH in net semi-exponential growth at higher

EC and lower pH values, as evidenced by the repeated peaks and troughs, with the highest vertex occurring at lower pH values. This trend seems logical according to known higher solubilities of calcium salts at lower pH values, coupled to reduced Ca^{2+} ion activities at higher concentrations of other soluble ions. At pH values higher than 7.5, a smoother correlation of Ca^{2+} ion concentrations with EC is evidenced, supporting the linearity portion in the scatter box plot matrix. The contour plot (Figure 14b) indicates the existence of pockets representing the highest calcium levels occurring at lower pH values and higher EC values.

3. NO_3^- has no geogenic or even known atmospheric sources in the region under study. NO_3^- exhibits a direct linear relationship with all other constituents at low levels, except HCO_3^-, which has inherent fluctuation pathways. Moreover, NO_3^- exhibits no trend for exchange or precipitation processes. Normality testing failed, with a p-value < 0.005, indicating the occurrence of unbalanced and localized accumulation processes. The probable processes include evaporation concentration, soil flush-out additions with subsequent nitrification, and seepages. The other additive process, nitrification, implies no direct, definite relationship with the other constituents, which may enable its basis for making judgements or comments. Evaporation concentration remains the most probable process to affect nitrate concentration in a localized fashion that impairs its normal distribution.
4. SO_4^{2-}, Cl^-, K^+, and Mg^{2+} exhibit similar linear trends in exacerbation, with the normality hypothesis rejected at p-values < 0.005, except that for SO_4^{2-}, which was retained but at very low p-value = 0.076.
5. SO_4^{2-} loads significantly contribute to the linear change in EC values with all major parameters, and quasi-inversely with pH, except HCO_3^-. This trend indicates that SO_4^{2-} was not significantly affected by the potential removal or attenuation processes, namely, ion exchange and precipitation. The study area contains many forms of sulfide minerals, including galena, sphalerite, polybasite, argentite, and pyrargirite, which, in their interaction with water, release SO_4^{2-} [32,59]. In addition, igneous and sedimentary rock sources, such as gypsum, and the anhydrite dissolution and redissolution of probable previous precipitates, if any, contribute to the load. The distribution map of sulfate ions (Figure 12c) clarifies that the wells saturated with sulfate lie in the northern and northeastern regions, agreeing with the general EC trend and surface morphometric levels. All these sources represent a plausible explanation for high loads of sulfate. However, the smooth trend in sulfate with other constituents indicates that it has a relatively common source and has undergone a co-occurring process, mostly evaporation. The 3D surface plot of its variation coupled with the conservative Cl^- ion and quasi-conservative sodium ion, for further investigation of the sulfate distribution, is portrayed in Figure 15b. The curves show that the sulfate ion concentration is directly propagated, i.e., the same as that of chloride and sodium. At the same time, the surface and contour maps of sulfate, calcium, and sodium show that sulfate is relatively inversely proportionate to calcium, especially at higher levels of sulfate. This behavior may be explained by the fact that the calcium precipitates as calcium carbonate, whereas the sulfate ion concentration propagates progressively, leading to the contouring of the semi-independence.
6. Low concentrations of sodium and calcium ions: Sodium and calcium ions show notably different themes with their ramping levels. At low concentration levels, up to 15 mEq/L each, a clear linear trend with a slope of ≈1 (Figure 16a) is evident. The chemical composition of the precipitation in the study area is not available; hence, the available average chemical composition of the precipitation in the nearest region with similar conditions, Riyadh, was used. The precipitation had consistent EC values of 300–400 µS/cm, with occasional incidents that had far higher EC values due to dissolution of the aerosol loads [60]. Precipitation chemical composition showed that the content (in epm) of Ca^{2+} is nearly six-fold that of Na^+. The study area samples are positioned on the equimolar line, demarcating a reasonable increase in Na^+ rel-

ative to, or perhaps at the expense of, Ca^{2+} ions. The potential pathways for such modifications include the occurrence of the ion exchange process, silicate weathering, and/or calcium salt precipitation. The question to be answered is, which process is the most probable or effective? To answer this question, at least asymptotically or conceptually, the authors looked for samples having similar chemical compositions to that of average precipitation. One sample from the study area, sample No. 14, which is located distant from farms and human activities, was used mainly for drinking; thus, the authors considered that it was only affected by the rock interactions, yielding a somewhat similar chemical composition with a slight increase in Na^+ content relative to that of Ca^{2+}. The equivalent ratios of Ca^{2+}/Na^+ decreased from 6 to 4.4, with a congruent increase in Cl^- confirming weathering of silicates; however, precipitation of calcium salts is still a potential process because the pH is 8.35. The EC value of sample No.14 was 255 µS/cm, which is very close to that of precipitation, corroborating the co-occurrence of potential calcium precipitation to compensate for that added by silicate weathering. The occurrence of ion exchange may lead to the same effects concerning sodium, but not for Cl^-, which increases slightly compared to sodium. The average chemical composition of precipitation contains equimolar amounts of Na^+ and Cl^- (0.269 and 0.267, respectively). Hence, the extent of ion exchange could be ascertained to be the tiny difference between Na^+ and Cl^- equivalent contents, of 0.07 mEq./L. If this sample is considered to be the baseline or datum, the effects of the processes, namely evaporation and human activities, can be accounted for, imagined, or even estimated quantitatively according to the availability of all other relevant information, to reduce the associated uncertainty budget as reasonably or practically as achievable.

7. Medium levels of sodium and calcium ions: At 15–30 mEq/L levels, a different theme to that mentioned in bullet point No. 6 appears to demarcate other relevant affecting processes. The points lie away from the equiline in the upper and lower directions. The lower-lying points represent increased Na^+ at the expense of Ca^{2+} ions due to ion exchange supported by the co-increase in sodium over chloride. On the contrary, the higher-lying points represent increased Ca^{2+} at the expense of Na^+ ions due to probable consecutive calcium concentrating processes. The former may represent calcium precipitation leading to reduced soluble calcium activity supplemented with reverse ion exchange, which yields lower Na^+ loads. The latter may be due to evaporation concentration at primarily reduced calcium activities and pH values, leading to an increase in calcium concentration. This trend overlays Cl^- and Na^+, supporting the fluctuation in Na^+ relevant to calcium, as shown in Figure 16a,b.
8. At far higher levels, >30 meq/L, the trend is still similar to that at the medium level, except the points are more distant as the height increases. This theme may be due to the rigorous effects of the vicious salinization cycle described in Scheme 1. Such effects require a continuous increase in Cl^- content relative to that of Ca^{2+}, as supported in the current findings (Figure 16c), and indicating the probable validity of the presented explanation. Moreover, to look further into the interrelationships among Cl^-, Ca^{2+}, and Na^+, a 3D surface plot is portrayed in Figure 16d. Calcium shows repeated peaks and troughs, confirming it underwent multiple processes compared to sodium and chloride, which show a relatively continuous increase. The largely peaked tail at the right corner confirms the absence or relief of calcium-lowering processes, such as precipitation, due to its lowered activity at the high concentrations of other ions. Additionally, the ion exchange may cease, reach a dynamic equilibrium state, or reverse due to high sodium levels.
9. HCO_3^- exhibits no definite pattern with all parameters, except with pH, which fluctuates sinusoidally. The normality test passed with the most significant *p*-value of 0.474, indicating no ultimate sink or source terms lead to net accumulation in a particular portion of the system. As pointed out and explained throughout this demonstration in different sections, HCO_3^- is continuously replenished and consumed at each ir-

rigation cycle. There was no net input of HCO_3^- due to the prevailing prolonged drought conditions. These trends are shown in Figure 17. As shown in Figure 17a, calcium shows an inverse relationship with HCO_3^-, denoting precipitation of calcium at higher HCO_3^-, or a less-affected well with irrigation water return flow, as in the case of low-EC water, and shown by the lower-right part of the 3D surface plot (Figure 17a). Ca^{2+} pockets appear at low levels of HCO_3^- and moderate to high levels of SO_4^{2-}, and become milder at higher HCO_3^- levels, as portrayed in the contour map (Figure 17b).

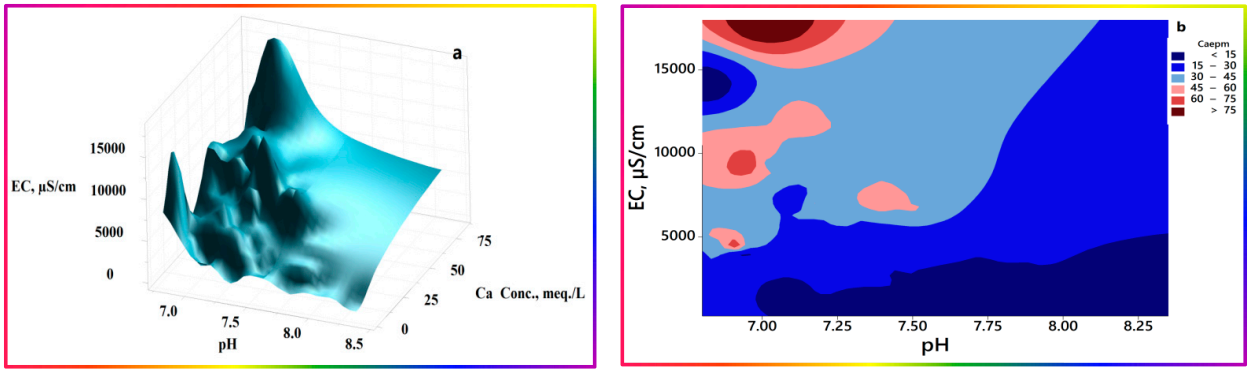

Figure 14. Three-dimensional surface (**a**) and contour plots (**b**) portray the interchanges among pH, EC, and Ca^{2+}. Ca^{2+} ion concentration expressed in milliEquivalents per liter (mEq/L), and EC in µS/cm.

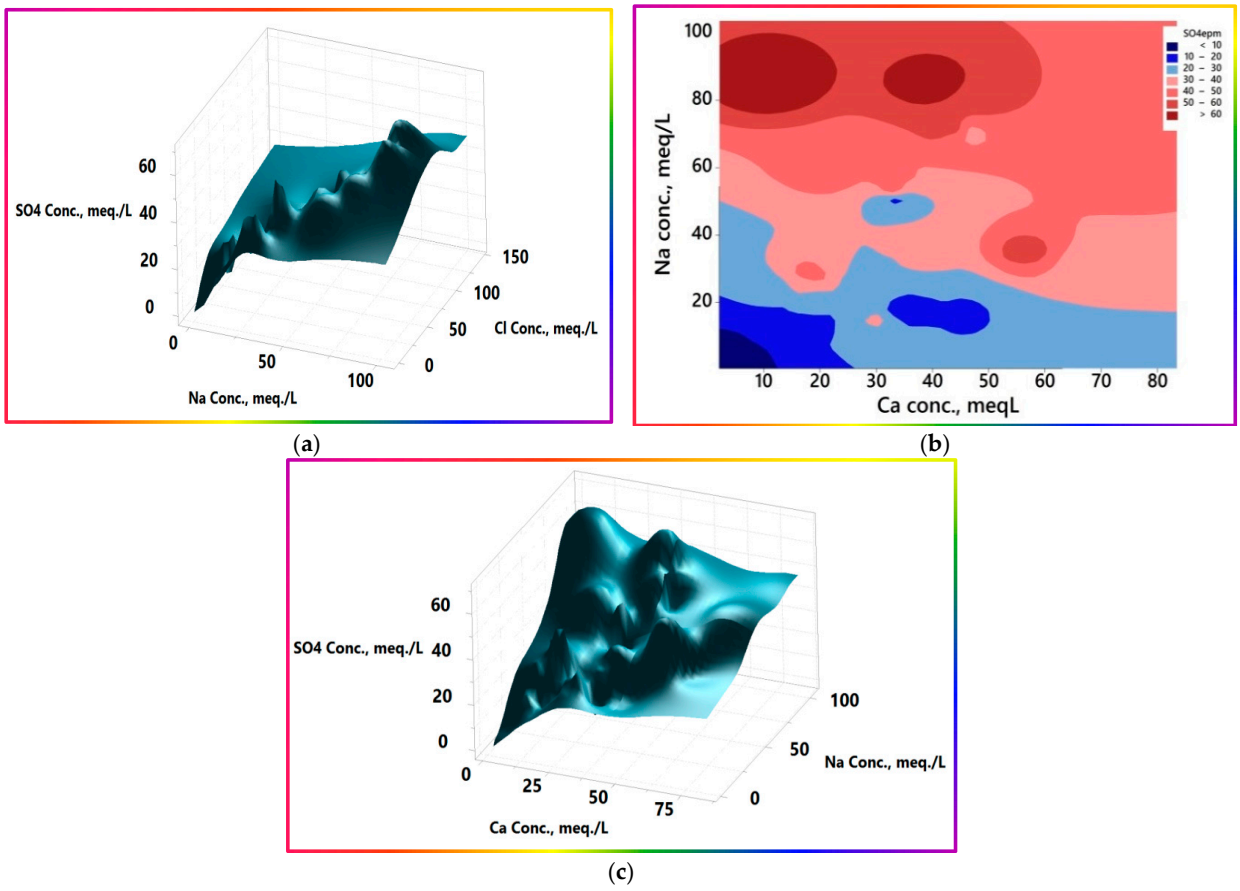

Figure 15. Three-dimensional surface plots and contour map of sulfate with Cl^-, Na^+, and Ca^{2+}. (**a**) 3D surface plotof SO_4^{2-}, Na^+, and Cl^- (**b**) Contour map of SO_4^{2-}, Na^+, and Ca^{2+} (**c**) 3D surface plotof SO_4^{2-}, Na^+, and Ca^{2+}.

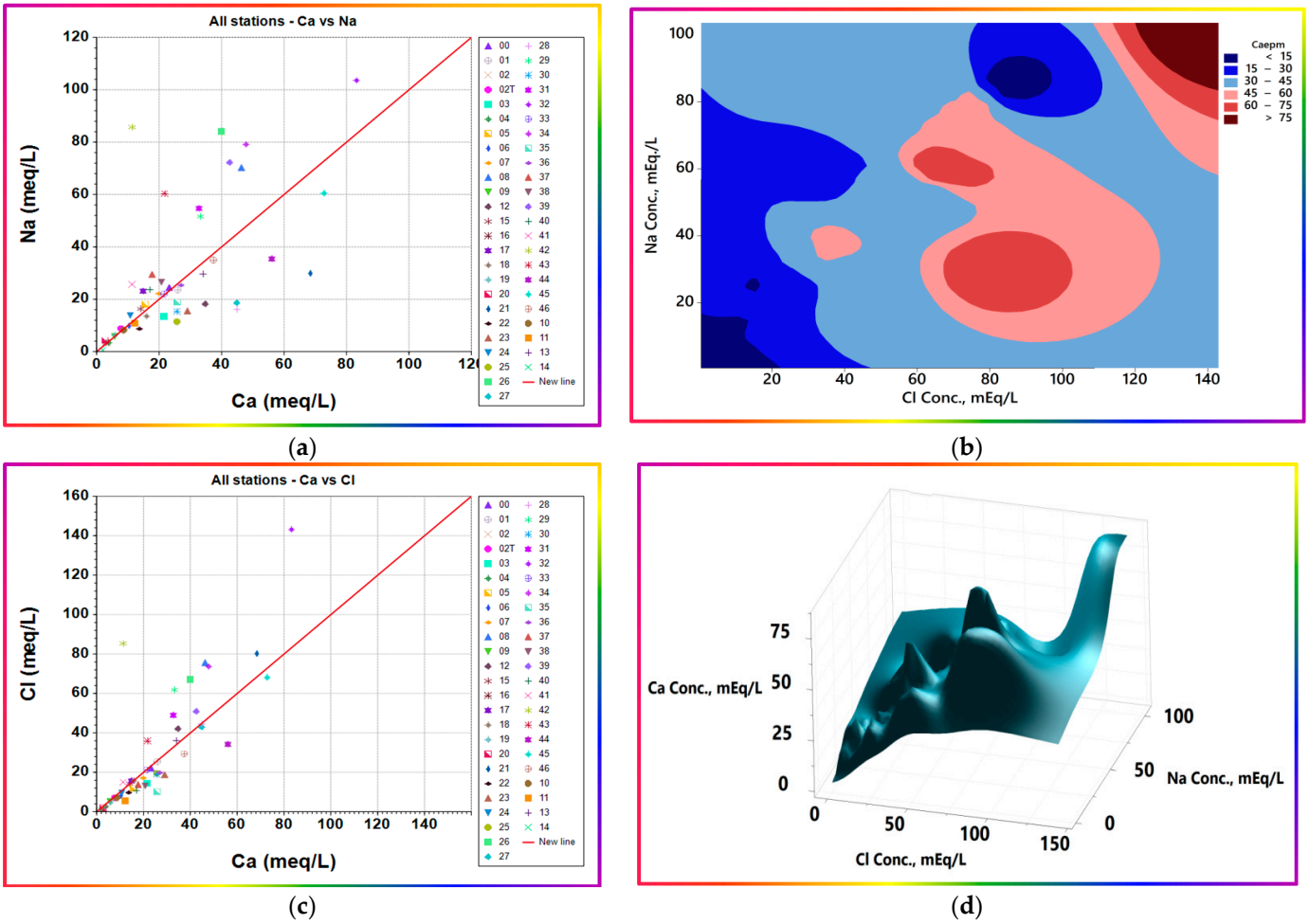

Figure 16. Ion ratio and 3D surface plots show Na^+, Ca^{2+}, and Cl^- interchanges. Na^+, Cl^-, and Ca^{2+} ion concentration expressed in mEq/L. (**a**) Ion ratio plot of Na^+ and Ca^{2+} (**b**) Contour plot of Ca^{2+} districbution with Na^+ and Cl^- (**c**) Ion ratio plot of Cl^- and Ca^{2+} (**d**) 3D surface plot of Ca^{2+}, Cl^-, and Na^+.

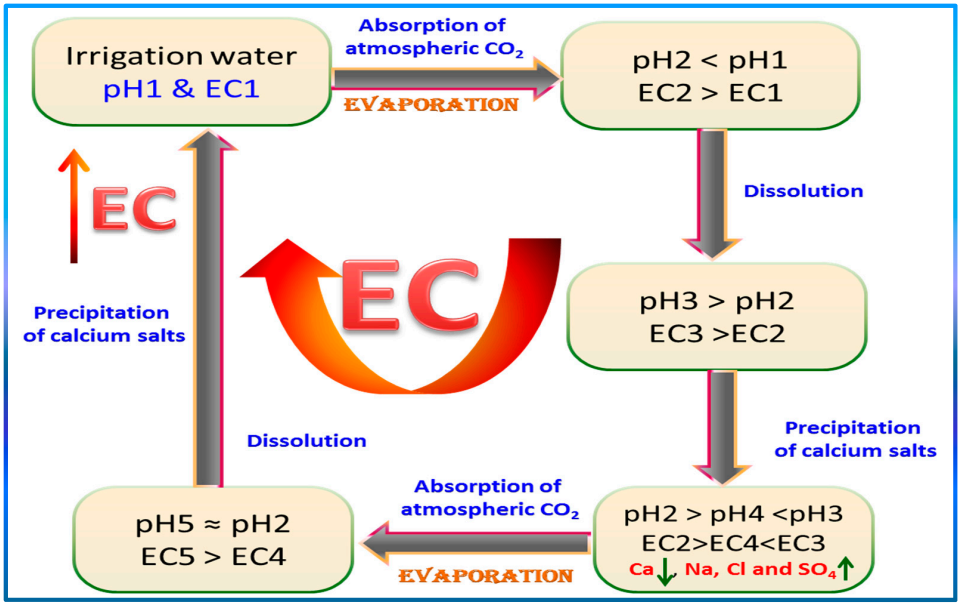

Scheme 1. Simplified proposed vicious cycle for the continuous salinization mechanism.

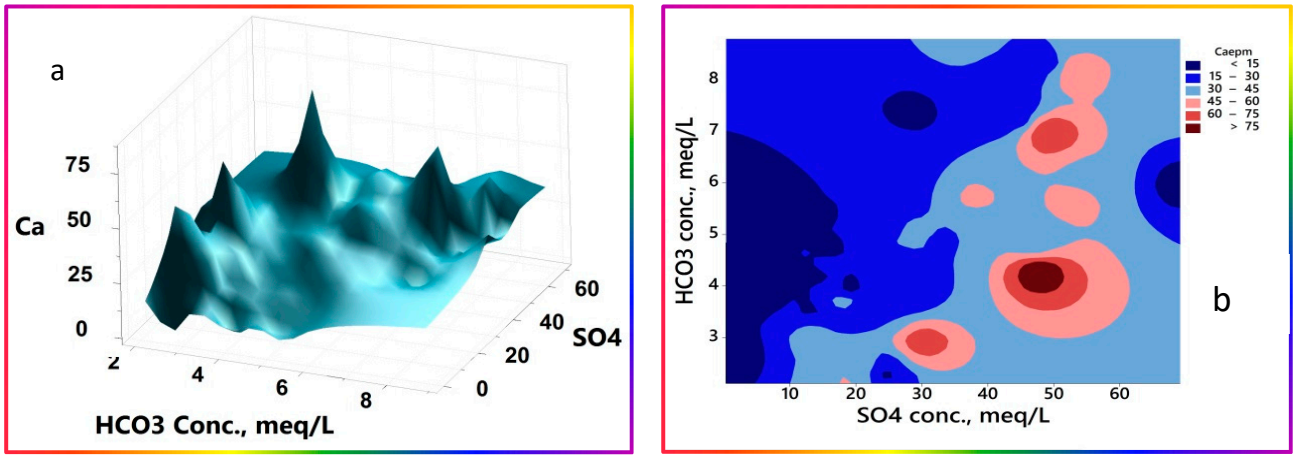

Figure 17. (**a**) 3D surface plot and contour map portraying the interchanges between SO_4^{2-}, Ca^{2+}, and HCO_3^-. (**b**) SO_4^{2-}, Ca^{2+}, and HCO_3^- ion concentration expressed in mEq/L.

3.5. Comparison with Gibbs Diagram

The hydrochemical properties of the water should be understood to identify the origin and the hydrochemical evolution of the GW. The Gibbs plot [26] has been commonly used to determine the hydrochemical processes that control GW chemistry. It was developed originally for surface water, and subsequently applied to GW. Some limitations for its application in GW studies were discussed extensively by [61]. The GW hydrogeochemistry is generally maintained through natural and anthropogenic sources that affect, or are controlled by, the physiochemical parameters. The Gibbs plot aids the understanding of the main factors' dominant role in maintaining hydrochemical water characteristics [8,26]. The Gibbs diagram is often employed to reflect the controlling effects of GW hydrochemical types (rock weathering, evaporation concentration, and precipitation). The water samples greatly affected by atmospheric precipitation are located in the lower corners; those controlled by rock weathering are located in the middle areas; whereas those controlled by evaporation crystallization are located in the upper corners. In order to compare the findings of this demonstration to the classically obtained results, the Gibbs diagram was drawn and discussed as a widely employed representative method for delineating the principal controlling processes [4,8,62–64]. The Gibbs diagram (Figure 18) emphasizes the evaporation dominance over the total salinity, with only one sample lying in the rock dominance region, i.e., sample No. 14. Although the Gibbs diagram results in the same conclusions as those mentioned above (evaporation dominance), it does not provide detailed insights into the nature and type of the influences, or into several easily identified, traced, and evidenced interconnected processes.

Marandi and Shand, 2018, discussed the concept and application limitations of the Gibbs diagram. They stated that it represents some of the key processes controlling surface water chemistry and may not accurately reflect those controlling most GW systems' chemistry. The modalities of several different processes may be masked, as only the ratios of $Na^+/(Na^+ + Ca^{2+})$ or $Cl^-/(Cl^- + HCO_3^-)$ are expressed. They concluded that using Gibbs graphs (1971), and particularly the boomerang shape and the placement of primary processes, may yield limited information, and their translations may oversimplify the interpretation of the aquifer systems and lead to relevant GW processes being overlooked [61].

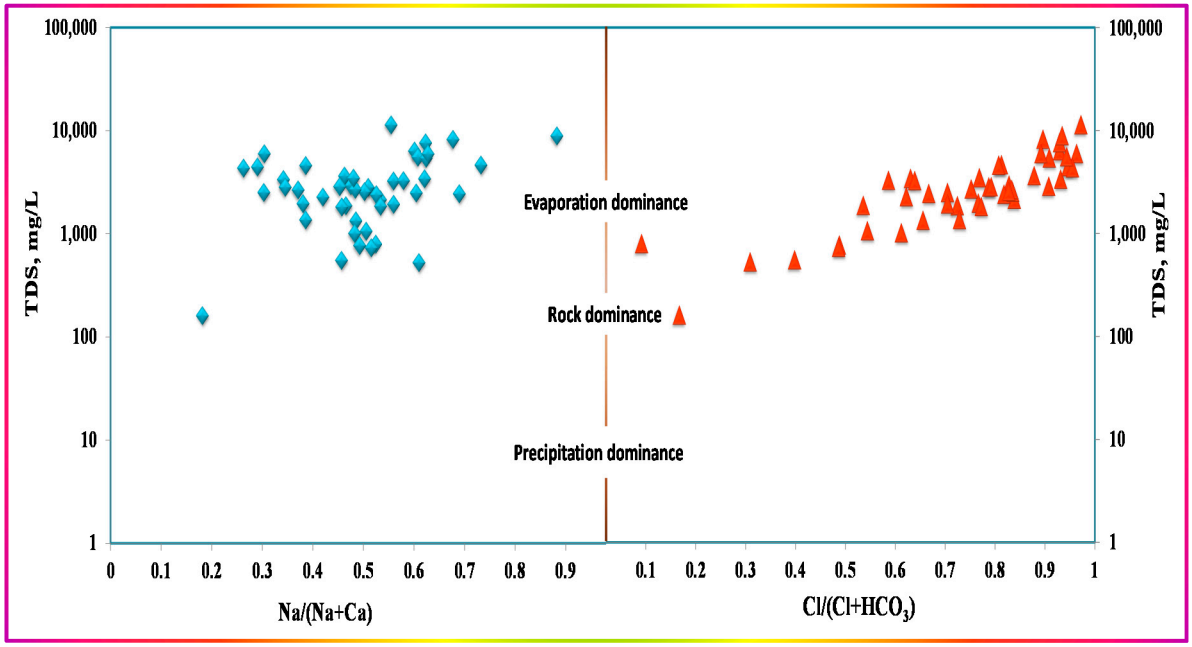

Figure 18. Gibbs diagram for the Ad-Dawadmi GW samples.

The visualization-based findings presented throughout this work agree with the Gibbs diagram, as evaporation is the primary process controlling the GW chemistry in the study area. However, other essential processes recognized by the visualization-based representations, such as direct and reverse ion exchange, precipitation of calcium salts, flushing out of soil-bounded salts, the role of HCO_3^- and pH fluctuations, and solution ion activities of calcium, cannot be inferred with the Gibbs diagram. These findings support the recommendations and criticism of Marandi and Shand, 2018 [61], of the Gibbs diagrams, and demonstrate the usefulness of the presented visualizations to guide reasonable interpretation and understanding of the system.

4. Conclusions

In the current work, the authors examined and assessed the practical application of many graphical methods to enhance data representation and analysis, to facilitate interpretation and obtain the relevant information of hydrogeochemical datasets. Among the study's many findings, the most important can be summarized as follows:

1. Overall, the evolution of the GW system in the Ad-Dawadmi study area is controlled by many co-occurring processes: aerosol dissolution, evaporation, direct and reverse ion exchange, precipitation of calcium salts, flushing out of soil-bounded salts, and rock weathering.
2. The major factors controlling the studied GW geochemistry are fluctuations in pH and HCO_3^- levels, coupled with evaporation.
3. The effects of prolonged drought and intensive human activities are the most severe factors responsible for the deterioration in the quality of the sole precious GW reserve in the study area.
4. Truncating the study area yielded helpful insights into major constituents' variation trends. In conclusion, the salinity increases from south to north and northeast, and from west to east, with remarkable changes in the distribution of major constituents, particularly sulfate, chloride, sodium, and calcium, in terms of both amount and proportion.
5. Essential processes recognized by the visualization-based representations, such as direct and reverse ion exchange, precipitation of calcium salts, flushing out of soil-

bounded salts, the role of HCO_3^- and pH fluctuations, and solution ion activities of calcium, cannot be inferred from the Gibbs diagram.

6. The integration of different visualizations that relate three parameters—bubble diagrams, 3D surface plots, and contour maps—was found to provide multiple lines of evidence, constrained interpretations, and insights that otherwise might be masked.
7. The scatter box plot matrix was found to be very useful, having the advantages of the collective representation of the whole spectrum of major ions on one plot, simplicity of production, presentation of extensive datasets on one graph, and direct readability.
8. Large SD values denote the significant variability within the area, which may be due to significant influencing parameters that are localized in nature, rather than effects of lithology, catchment-wise, or basin-wise processes.
9. Pockets of higher EC values, NO_3^-, SO_4^{2-}, Cl^-, Na^+, and Ca^{2+} are remarkable, indicating the effects of point source activities, primarily agriculture and livestock farming.
10. The vicious salinization cycle was devised and illustrated in the simplified Scheme 1, and is thought to be the process causing the worst deterioration in the GW quality and the salinity within the study area.

Author Contributions: Conceptualization, H.E.G., A.A.A. and F.A.G.; methodology, H.E.G., M.C., A.A.A. and F.A.G.; software, H.E.G. and F.A.G.; validation, A.A.A., A.H.A. and M.C.; formal analysis, H.E.G., A.H.A. and M.C.; investigation, H.E.G., A.H.A. and F.A.G.; resources, A.A.A. and H.E.G.; data curation, A.A.A. and F.A.G.; writing—original draft preparation, H.E.G. and F.A.G.; writing—review and editing, A.A.A., M.C. and A.H.A.; visualization, H.E.G. and F.A.G.; supervision, H.E.G.; project administration, H.E.G.; funding acquisition, H.E.G. All authors have read and agreed to the published version of the manuscript.

Funding: The authors extend their appreciation to the Deputyship for Research & Innovation, Ministry of Education in Saudi Arabia, for funding this research work through the project number (IFP2021-062).

Institutional Review Board Statement: Not applicable.

Informed Consent Statement: Not applicable.

Data Availability Statement: Not applicable.

Conflicts of Interest: The authors declare no conflict of interest. The funders had no role in the design of the study; in the collection, analyses, or interpretation of data; in the writing of the manuscript, or in the decision to publish the results.

References

1. Silva, M.I.; Gonçalves, A.M.L.; Lopes, W.A.; Lima, M.T.V.; Costa, C.T.F.; Paris, M.; Firmino, P.R.A.; De Paula Filho, F.J. Assessment of Groundwater Quality in a Brazilian Semiarid Basin Using an Integration of GIS, Water Quality Index, and Multivariate Statistical Techniques. *J. Hydrol.* **2021**, *598*, 126346. [CrossRef]
2. Bozdağ, A. Assessment of the Hydrogeochemical Characteristics of Groundwater in Two Aquifer Systems in Çumra Plain, Central Anatolia. *Environ. Earth Sci.* **2016**, *75*, 674. [CrossRef]
3. Benaafi, M.; Al-shaibani, A. Hydrochemical and Isotopic Investigation of the Groundwater from Wajid Aquifer in Wadi Al-Dawasir, Southern Saudi Arabia. *Water* **2021**, *13*, 1855. [CrossRef]
4. Ren, C.; Zhang, Q. Groundwater Chemical Characteristics and Controlling Factors in a Region of Northern China with Intensive Human Activity. *Int. J. Environ. Res. Public Health* **2020**, *17*, 9126. [CrossRef] [PubMed]
5. Jha, M.K.; Shekhar, A.; Jenifer, M.A. Assessing Groundwater Quality for Drinking Water Supply Using Hybrid Fuzzy-GIS-Based Water Quality Index. *Water Res.* **2020**, *179*, 115867. [CrossRef]
6. Saleem, Q.M.; Algamal, Y. Assessment of Physico-Chemical and Biological Properties of Ground Water of Khulais, Province, Kingdom of Saudi Arabia. *Int. J. Sci. Res. Methodol.* **2016**, *5*, 504–521.
7. Su, Y.-H.; Feng, Q.; Zhu, G.-F.; Si, J.-H.; Zhang, Y.-W. Identification and Evolution of Groundwater Chemistry in the Ejin Sub-Basin of the Heihe River, Northwest China. *Pedosphere* **2007**, *17*, 331–342. [CrossRef]
8. Kumar, P.; Mahajan, A.K.; Kumar, A. Groundwater Geochemical Facie: Implications of Rock-Water Interaction at the Chamba City (HP), Northwest Himalaya, India. *Environ. Sci. Pollut. Res.* **2020**, *27*, 9012–9026. [CrossRef]
9. Dehnavi, A.; Sarikhani, R.; Nagaraju, D. Hydro Geochemical and Rock Water Interaction Studies in East of Kurdistan, NW of Iran. *Int. J. Environ. Sci. Res.* **2011**, *1*, 16–22.

10. Subramani, T.; Rajmohan, N.; Elango, L. Groundwater Geochemistry and Identification of Hydrogeochemical Processes in a Hard Rock Region, Southern India. *Environ. Monit. Assess.* **2010**, *162*, 123–137. [CrossRef]
11. Hanshaw, B.B.; Back, W. Major geochemical processes in the evolution of carbonate—Aquifer systems. *J. Hydrol.* **1979**, *43*, 287–312. [CrossRef]
12. Ahmed, M.A. *Study of Genesis and Quality of Groundwater in The Northern Part of Upper Egypt Using Chemical and Environmental Isotopes Techniques*; Cairo University: Cairo, Egypt, 2002.
13. Dohare, D.; Deshpande, S.; Kotiya, A. Analysis of Ground Water Quality Parameters: A Review. *Res. J. Eng. Sci. ISSN* **2014**, *2278*, 9472.
14. Kachroud, M.; Trolard, F.; Kefi, M.; Jebari, S.; Bourrié, G. Water Quality Indices: Challenges and Application Limits in the Literature. *Water* **2019**, *11*, 361. [CrossRef]
15. Pourcq, K.D. Elements for a Methodology to Interpret Hydrochemichal Data. 2008. Available online: https://upcommons.upc.edu/handle/2099.1/6434 (accessed on 9 May 2022).
16. Herczeg, A.L.; Dogramaci, S.S.; Leaney, F.W.J. Origin of Dissolved Salts in a Large, Semi-Arid Groundwater System: Murray Basin, Australia. *Mar. Freshw. Res.* **2001**, *52*, 41–52. [CrossRef]
17. Glynn, P.D.; Plummer, L.N. Geochemistry and the Understanding of Ground-Water Systems. *Hydrogeol. J.* **2005**, *13*, 263–287. [CrossRef]
18. Chandrasekaran, S.; Sankaran Pillai, G.; Venkatraman, B. Spatial and Heavy Metal Assessment in Beach Sands of East Coast of Tamil Nadu, India. *Environ. Nanotechnol. Monit. Manag.* **2020**, *14*, 100324. [CrossRef]
19. Lu, W.; Sarkar, A.; Hou, M.; Liu, W.; Guo, X.; Zhao, K.; Zhao, M. The Impacts of Urbanization to Improve Agriculture Water Use Efficiency—An Empirical Analysis Based on Spatial Perspective of Panel Data of 30 Provinces of China. *Land* **2022**, *11*, 80. [CrossRef]
20. Joodavi, A.; Aghlmand, R.; Podgorski, J.; Dehbandi, R.; Abbasi, A. Characterization, Geostatistical Modeling, and Health Risk Assessment of Potentially Toxic Elements in Groundwater Resources of Northeastern Iran. *J. Hydrol. Reg. Stud.* **2021**, *37*, 100885. [CrossRef]
21. Zakaria, N.; Anornu, G.; Adomako, D.; Owusu-Nimo, F.; Gibrilla, A. Evolution of Groundwater Hydrogeochemistry and Assessment of Groundwater Quality in the Anayari Catchment. *Groundw. Sustain. Dev.* **2021**, *12*, 100489. [CrossRef]
22. Elmeknassi, M.; El Mandour, A.; Elgettafi, M.; Himi, M.; Tijani, R.; El Khantouri, F.A.; Casas, A. A GIS-Based Approach for Geospatial Modeling of Groundwater Vulnerability and Pollution Risk Mapping in Bou-Areg and Gareb Aquifers, Northeastern Morocco. *Environ. Sci. Pollut. Res.* **2021**, *28*, 51612–51631. [CrossRef]
23. Liaqat, M.U.; Mohamed, M.M.; Chowdhury, R.; Elmahdy, S.I.; Khan, Q.; Ansari, R. Impact of Land Use/Land Cover Changes on Groundwater Resources in Al Ain Region of the United Arab Emirates Using Remote Sensing and GIS Techniques. *Groundw. Sustain. Dev.* **2021**, *14*, 100587. [CrossRef]
24. Mandel, S.; Shiftam, Z.L.; Hamill, L.; Bell, F.G.; Ingraham, N.L.; Caldwell, E.A.; Verhagen, B.T.; Finkelman, R.B.; Orem, W.H.; Plumlee, G.S.; et al. Sustainability of Morocco's Groundwater Resources in Response to Natural and Anthropogenic Forces. *J. Hydrol.* **2021**, *603*, 106795. [CrossRef]
25. Khan, A.; Khan, H.H.; Umar, R.; Khan, M.H. An Integrated Approach for Aquifer Vulnerability Mapping Using GIS and Rough Sets: Study from an Alluvial Aquifer in North India. *Hydrogeol. J.* **2014**, *22*, 1561–1572. [CrossRef]
26. Gibbs, R.J.; Feth, J.H. Mechanisms Controlling World Water Chemistry: Evaporation-Crystallization Process. *Am. Assoc. Adv. Sci. Stable* **1971**, *172*, 870–872. [CrossRef]
27. AdDawadmi_Gover. Available online: https://ar.wikipedia.org/wiki/%D9%85%D8%AD%D8%A7%D9%81%D8%B8%D8%A9_%D8%A7%D9%84%D8%AF%D9%88%D8%A7%D8%AF%D9%85%D9%8A (accessed on 12 March 2022).
28. SSYB. Annual Yearbook | General Authority for Statistics. 2010. Available online: https://www.stats.gov.sa/en/46 (accessed on 9 May 2022).
29. Al-Zaidi, A.A.; Elhag, E.A.; Al-Otaibi, S.H.; Baig, M.B. Negative Effects of Pesticides on the Environment and the Farmers Awareness in Saudi Arabia: A Case Study. *J. Anim. Plant Sci.* **2011**, *21*, 605–611.
30. El-Didy, S. Evaluation of The Proposed Drainage Network for Lowering the Groundwater Levels in Al-Dawadmi Town. *J. King Abdulaziz Univ. Environ. Arid L. Agric. Sci.* **1997**, *8*, 111–123. [CrossRef]
31. Johnson, P.R. Explanatory Notes To the Map of Proterozoic Geology of Western Saudi Arabia. 2006. Available online: https://instruct.uwo.ca/earth-sci/fieldlog/pan_african/Nubian/saudi/Explanatory%20notes%20for%20the%20shield%20SGS-TR-2006-4.pdf (accessed on 9 May 2022).
32. Al Shanti, M.S. The Geology and Mineralization of the AdDawadmi District of Saudi Arabia. Ph.D. Thesis, Imperial College London, London, UK, 1973.
33. Timeanddate Climate and Weather Averages in Ad Dawadmi, Saudi Arabia. Available online: https://www.timeanddate.com/weather/saudi-arabia/dawadmi/climate (accessed on 12 March 2022).
34. Quevauviller, P.; Thompson, K.C. *Analytical Methods for Drinking Water*; John Wiley & Sons: New York, NY, USA, 2005; ISBN 9780470094938.
35. DPIR. Methodology for the Sampling of Surface Water. *North. Territ. Gov.* **1998**, *11*, 1–11.
36. USGS. *National Field Manual for the Collection of Water-Quality Data. U.S. Geological Survey Techniques of Water-Resources Investigations, Book 9*; USGS: Preston, VA, USA, 2015.

37. APHA. *Standard Methods: For the Examination of Water and Waste Water*, 23rd ed.; Baird, R., Eaton, A., Rice, E., Eds.; American Public Health Association: Washington, DC, USA, 2017.
38. Hussein, R.A. *Study on Some Sources of Nitrate Pollution in Water Using Nitrogen-15 Isotope Technique*; Ain Shams University: Cairo, Egypt, 2005.
39. Middleton, K.R. A New Procedure for Rapid Determination of Nitrate and a Study of the Preparation of the Phenol-Sulphonic Acid Reagent. *J. Appl. Chem.* **1958**, *8*, 505–509. [CrossRef]
40. Ahmed, M.A.; Aly, A.I.; Gomaa, H.E.; Bastaweesy, A.M. Modified Low-Priced Ammonia Diffusion Method for the Analysis of Nitrogen Isotopic Composition of Ammonium and Nitrate in Different Water Matrices. *Egypt. J. Radiat. Sci. Appl.* **2008**, *21*, 257–281.
41. Paul Bourke Interpolation Methods. Available online: http://paulbourke.net/miscellaneous/interpolation/ (accessed on 14 March 2022).
42. Will Kenton Interpolation Definition. Available online: https://www.investopedia.com/terms/i/interpolation.asp (accessed on 14 March 2022).
43. Ahmad, A.Y.; Al-Ghouti, M.A.; Khraisheh, M.; Zouari, N. Hydrogeochemical Characterization and Quality Evaluation of Groundwater Suitability for Domestic and Agricultural Uses in the State of Qatar. *Groundw. Sustain. Dev.* **2020**, *11*, 100467. [CrossRef]
44. Komisarek, J. Groundwater Chemistry and Hydrogeochemical Processes in a soil catena of the poznań lakeland. *J. Elem.* **2017**, *22*, 681–695. [CrossRef]
45. Mallick, J.; Singh, C.K.; Al Mesfer, M.K.; Kumar, A.; Khan, R.A.; Islam, S.; Rahman, A. Hydro-Geochemical Assessment of Groundwater Quality in Aseer Region, Saudi Arabia. *Water* **2018**, *10*, 1847. [CrossRef]
46. Arslan, A.; Dutt, G.R. Solubility of Gypsum and Its Prediction in Aqueous Solutions of Mixed Electrolytes. *Soil Sci.* **1993**, *155*, 37–47. [CrossRef]
47. Azaza, H.; Mechi, L.; Doggaz, A.; Optasanu, V.; Tlili, M.; Amor, M. Ben Calcite and Barite Precipitation in CaCO3-BaSO4-NaCl and BaSO4-NaCl-CaCl2 Aqueous Systems: Kinetic and Microstructural Study. *Arab. J. Geosci.* **2017**, *10*, 1–9. [CrossRef]
48. Azimi, G.; Papangelakis, V.G. Chemical Modelling of Calcium Sulphate Phase Equilibria in Multicomponent Electrolyte Solutions. *AIChE Annu. Meet. Conf. Proc.* **2008**, *4*, 1–12.
49. Van Driessche, A.E.S.; Stawski, T.M.; Benning, L.G.; Kellermeier, M. Calcium Sulfate Precipitation Throughout Its Phase Diagram. *New Perspect. Miner. Nucleation Growth* **2017**, 227–256. [CrossRef]
50. Al Suhaimi, A.O.; Al Mohaimidi, K.M.; Momani, K.A. Preliminary Assessment for Physicochemical Quality Parameters of Groundwater in Oqdus Area, Saudi Arabia. *J. Saudi Soc. Agric. Sci.* **2019**, *18*, 22–31. [CrossRef]
51. Hwang, J.Y.; Park, S.; Kim, H.-K.; Kim, M.-S.; Jo, H.-J.; Kim, J.-I.; Lee, G.-M.; Shin, I.-K.; Kim, T.-S. Hydrochemistry for the Assessment of Groundwater Quality in Korea. *J. Agric. Chem. Environ.* **2017**, *6*, 1–29. [CrossRef]
52. Rezaei, A.; Hassani, H. Hydrogeochemistry Study and Groundwater Quality Assessment in the North of Isfahan, Iran. *Environ. Geochem. Health* **2018**, *40*, 583–608. [CrossRef]
53. Elnazer, A.A.; Seleem, E.M.M.; Zeid, S.A.M.; Ismail, I.S.A.; Bahlol, H.A.; Salman, S.A. Hydrochemical Evaluation of the Quaternary Aquifer and Its Suitability for Different Purposes at South Al Waqf City, Qena, Upper Egypt. *Groundw. Sustain. Dev.* **2021**, *12*, 100517. [CrossRef]
54. Sutadian, A.D.; Muttil, N.; Yilmaz, A.G.; Perera, B.J.C. Development of River Water Quality Indices—A Review. *Environ. Monit. Assess.* **2016**, *188*, 58. [CrossRef] [PubMed]
55. Gurunadha Rao, V.V.S.; Tamma Rao, G.; Surinaidu, L.; Mahesh, J.; Mallikharjuna Rao, S.T.; Mangaraja Rao, B. Assessment of Geochemical Processes Occurring in Groundwaters in the Coastal Alluvial Aquifer. *Environ. Monit. Assess.* **2013**, *185*, 8259–8272. [CrossRef] [PubMed]
56. Minitab Support System The Anderson-Darling Statistic—Minitab. Available online: https://support.minitab.com/en-us/minitab/18/help-and-how-to/statistics/basic-statistics/supporting-topics/normality/the-anderson-darling-statistic/ (accessed on 17 March 2022).
57. Anderson-Darling Normality Test. Available online: https://variation.com/wp-content/distribution_analyzer_help/hs140.htm (accessed on 15 March 2022).
58. Anderson-Darling Test for Normality | BPI Consulting. Available online: https://www.spcforexcel.com/knowledge/basic-statistics/anderson-darling-test-for-normality (accessed on 15 March 2022).
59. Moore, J.M.; Shanti, A.M.A.L. The Use of Stress Trajectory Analysis in the Elucidation of Part of the Najd Fault System, Saudi Arabia. *Proc. Geol. Assoc.* **1973**, *84*, 383–403. [CrossRef]
60. Michelsen, N.; Reshid, M.; Siebert, C.; Schulz, S.; Knöller, K.; Weise, S.M.; Rausch, R.; Al-Saud, M.; Schüth, C. Isotopic and Chemical Composition of Precipitation in Riyadh, Saudi Arabia. *Chem. Geol.* **2015**, *413*, 51–62. [CrossRef]
61. Marandi, A.; Shand, P. Groundwater Chemistry and the Gibbs Diagram. *Appl. Geochem.* **2018**, *97*, 209–212. [CrossRef]
62. Lakshmanan, E.; Kannan, R.; Senthil Kumar, M. Major Ion Chemistry and Identification of Hydrogeochemical Processes of Ground Water in a Part of Kancheepuram District, Tamil Nadu, India. *Environ. Geosci.* **2003**, *10*, 157–166. [CrossRef]

63. Masoud, A.A.; Aldosari, A.A. Groundwater Quality Assessment of a Multi-Layered Aquifer in a Desert Environment: A Case Study in Wadi Ad-Dawasir, Saudi Arabia. *Water* **2020**, *12*, 3020. [CrossRef]
64. Subba Rao, N.; Marghade, D.; Dinakar, A.; Chandana, I.; Sunitha, B.; Ravindra, B.; Balaji, T. Geochemical Characteristics and Controlling Factors of Chemical Composition of Groundwater in a Part of Guntur District, Andhra Pradesh, India. *Environ. Earth Sci.* **2017**, *76*, 747. [CrossRef]